International Journal of Engineering Science 163 (2021) 103472

Contents lists available at ScienceDirect

International Journal of Engineering Science

journal homepage: www.elsevier.com/locate/ijengsci

Mechanics of a pressurized penny-shaped crack in a poroelastic halfspace

A.P.S. Selvadurai*, P. Samea

Department of Civil Engineering and Applied Mechanics, McGill University, 817 Sherbrooke Street West, Montréal, QC H3A 0C3, Canada

ARTICLE INFO

Article history:
Received 6 December 2020
Revised 6 March 2021
Accepted 10 March 2021

Keywords:
Biot poroelasticity
Penny-shaped crack in a halfspace
Fluid injection
Integral transform techniques
Coupled Fredholm integral equations of the second-kind
Time-dependent stress intensity factors (SIFs)

ABSTRACT

This paper examines the axisymmetric problem of a penny-shaped crack located in a poroelastic halfspace that is modelled by Biot poroelasticity. The paper first examines the axisymmetric problem of the mechanics of fluid injection over a circular area within a halfspace that would create the skeletal stress state necessary to initiate fracture. The triggering of the fracture is assumed to create an axisymmetric penny-shaped crack whose surfaces will be subjected to fluid pressure. The mechanics of the penny-shaped crack in terms of its potential to extend in an axisymmetric fashion is examined by formulating the poroelastic mixed boundary value problem and solving the coupled Fredholm integral equations of the second-kind obtained through successive applications of integral transform techniques. The analysis of the poroelasticity problem of fluid-injection into the crack gives rise to time-dependent skeletal stress intensity factors (SIFs) at the crack tip; these are combined with a mixed-mode brittle skeletal fracture criterion to establish the injection pressures that can lead to the extension of the penny-shaped crack in a self-similar fashion.

1. Introduction

Our understanding of the role of cracks, inhomogeneities and other defects in the initiation and progression of failure in solid materials has a long history dating back to the classical studies in linear elastic fracture mechanics modelling proposed by Griffith (1921, 1924) and the theoretical foundations of stress concentrations around cavities and defects in elastic media developed by Inglis (1913), Kolosov (1935), Muskhelishvili (1953), Westergaard (1939) and others. The literature related to fracture mechanics of elastic solids can be found in an extensive collection of journals, volumes and texts and no attempt will be made to provide an up-to-date review (see e.g. Atkinson, 1979; Barenblatt, 1962; Cottrell, 1965; Eshelby, 1957; Goodier, 1933; Hellan, 1985; Hills et al., 1996; Kassir & Sih, 1975; Lawn & Wilshaw, 1975; Liebowitz, 1968; Popelar & Kanninen, 1985; Selvadurai, 2020; Sih, 1991; Sinclair, 2004a, 2004b; Sneddon, 1946, 1965; Sneddon & Lowengrub, 1969; Spencer, 1965; Sternberg, 1958; Willis, 1967). Studies in linear elastic fracture mechanics are of particular interest to the fracture mechanics of fluid-saturated brittle elastic materials since limiting solutions of the analogous poroelasticity problem at *zero time* and at *infinite time* can be recovered as special cases of the linear elasticity solutions. The investigations in the area of linear elastic fracture mechanics have also been extended to include crack initiation, crack extension, dynamic crack propagation, crack branching and crack coalescence (Aliabadi, 1997; Broberg, 1999; Broek, 1982; Cherepanov, 1979; Guéguen & Kachanov, 2011; Kachanov, 1992; Sanford, 1997; Selvadurai, 2000; Selvadurai, 2006; Selvadurai & ten Busschen, 1995; Selvadurai et al., 1996; Selvadurai et al., 2005; Sih & Chen, 1981). The work on linear elastic fracture mechanics

* Corresponding author.
E-mail addresses: patrick.selvadurai@mcgill.ca (A.P.S. Selvadurai), parham.samea@mail.mcgill.ca (P. Samea).

https://doi.org/10.1016/j.ijengsci.2021.103472
0020-7225/

has also been extended to include elastic-plastic and viscoelastic material behaviour (Francis et al., 1974; Knauss, 1970; Schapery, 1975; Selvadurai, 1992; Selvadurai et al., 1990). Of particular interest to the scope of this paper are studies dealing with brittle geomaterials including rocks and concrete, that have been extensively studied in the context of elasticity, crack initiation, friction at crack surfaces and damage mechanics (Bazant, 1981; Bazant & Planas, 1998; Brace, 1960; Brace & Bombalakis, 1963; Elfgren, 1989; Jaeger, 1971; Kachanov et al., 2013; Karihaloo, 1995; Krajcinovic, 1984; Maier et al., 2006; McClintock & Walsh, 1962; Murrell, 1962; Rossmanith, 1983; Shah et al., 1989; Shah et al., 1989; Shen et al., 2014). Again, the articles covering these topics are too numerous to cite individually and the cited references can be consulted for further information.

The present article examines the class of problems in fracture mechanics that are of interest to earth sciences, environmental geomechanics and resource geomechanics. The topic of the mechanics of pre-existing fractures in fluid-saturated rocks is of interest to branches of geodynamics dealing with fault movement and earthquake processes. The incorporation of poroelastic modelling of the problem in terms of a complete analysis of a transient problem based on Biot's theory of poroelasticity (Biot, 1941, 1956) is rare and important studies in this area have been conducted by Rice and Cleary (1976) dealing with continuous distributions of dislocations in poroelastic media to examine two-dimensional stable cracks. The work was extended by Cleary (1977), Rice and Simons (1976), Rudnicki (1980, 1984, 1996), Rudnicki and Roeloffs (1990) and others to examine the role of coupled poroelastic effects on the extension and propagation of defects in poroelastic media. Further applications of these developments to coupled poroelastic processes resulting from magma intrusion have also been investigated by Ellsworth et al. (1996).

The subject of crack initiation and extension in fluid-saturated poroelastic media has acquired some importance in connection with the injection of fluids, such as fluidized greenhouse gases and hazardous fluids, to ameliorate the effects of climate change and techniques used to enhance extraction of energy resources related to geothermal energy and oil and gas recovery. In connection with the sequestration of greenhouse gases (GHGs), the objective is to inject the fluidized GHGs without damage to either the storage formation or to the caprock strata that facilitates the development of a buoyant plume. The complete problem involves consideration of thermo-poromechanical effects (Chan & Stanchell, 2009; Khalili & Selvadurai, 2003; McTigue, 1986; Rutqvist & Tsang, 2002; Selvadurai & Najari, 2017; Selvadurai & Nguyen, 1995, 1997; Selvadurai & Suvorov, 2012, 2014, 2016a; Tsang et al., 2009) and the application to geologic sequestration issues requires further study. The pressurization of elastic formations underlain by caprock has been investigated in Zheltov and Khristianovitch (1955), and Selvadurai and Kim (2016). The isothermal mathematical modelling of the near surface injection of fluids into a potential poroelastic storage formation overlain by a caprock was investigated by Khristianovitch and Zheltov (1955). By its very nature, the mathematical modelling lends itself to only highly idealized formulations of the problem involving axial symmetry, defect-free homogeneous poroelastic media and pre-identified injection zones. In the context of applications to resources extraction, either geothermal or oil and gas exploration, the basic issues that need to be addressed are: (i) Under what conditions will a crack form or nucleate at a location in an *initially geostatically pre-loaded* geologic formation? (ii) Once a defect is formed, what conditions promote the progress of the formed crack in either a controlled (steady) or uncontrolled (unsteady) extension? (iii) Can the extension path of the created crack be predicted? (iv) What roles do defects and inhomogeneities play in the formation and extension of cracks? (v) What roles do poroelasticity or thermo-poroelasticity play in the identification of crack nucleation, crack extension, crack branching and crack arrest? The answers to these issues are yet to be examined in a comprehensive manner. Whether there will be approaches that can address all these issues is also a debatable point. What is conceived as an idealized model can be far removed from the actual manifestations. Early analysis of hydraulic fracture endeavours was largely restricted to modelling by appeal to linear elastic fracture models. The classical studies by Barenblatt (1956, 1957, 1959), Cleary (1979, 1980, Clifton and Abou-Sayed (1979), Daneshy (1973, 1978), Geertsma and Haafkens (1979), Howard and Fast (1970), Le Tirant and Dupuy (1967), Nordgren (1972), Perkins and Kern (1961)), and Nemat-Nasser et al. (1983) are recognized for their noteworthy fundamental contributions to the development and understanding of the subject. Other work summarizing the advances in the application of hydraulic fracturing to resources exploration and geothermal energy extraction were given by Adachi and Detournay (2008), Cherepanov (2015), Desroches et al. (1994), Ma and Holditch (2016), Mader (1989), Mendelsohn (1984a,1984b), Savitski and Detournay (2002), Smith (2015), Speight (2016), Valko and Economides (1996), and Selvadurai (2019a). Of related interest are the type of hydraulic fracturing models that consider pseudo-poroelastic mechanics of hydraulic fracture. In these studies, the analysis is largely restricted to linear elastic behaviour of a solid containing a specified crack and attention is focused on the mechanics of fluid flow within the fracture. The fluid itself can have viscosity effects and allowance is also made to account for fluid leakage into a purely elastic porous medium. Examples of studies in this area are given by Hu and Garagash (2010), Kanin et al. (2020), Lecampion et al. (2018) and Williams (1970). There are several studies that investigate the process of crack extension in brittle elastic media through the incorporation of computational approaches to modelling, including finite element schemes, boundary element schemes and, more recently, the application of X-FEM and level-set techniques (Chau et al., 2016; Cheng and Predeleanu, 1987; Csati et al., 2020; Dargush & Banerjee, 1991; De Borst et al., 2006; Dong & Atluri, 2013a, 2013b; Massart & Selvadurai, 2012, 2014; Miehe & Mauthe, 2016; Moës & Belytschko, 2002; Moës et al., 1999; Rajapakse & Senjuntichai, 1995; Réthoré et al., 2007; Salimzadeh et al., 2017; Sandhu & Wilson, 1969; Selvadurai et al., 2015; Yi et al., 2020; Zienkiewicz & Shiomi, 1984). The extension of these concepts to consider poroelastic coupling with the examination of crack extension, crack branching and multiple crack initiation during the hydraulic fracture development requires the application of advanced computational approaches.

The systematic mathematical studies of the plane strain dynamical response of cracks in poroelastic media were given by Atkinson and Craster (1991, 1995) and Craster and Atkinson (1996) and these analytical solutions have been used as benchmarks to validate computational approaches for examining crack extension in poroelastic media (Selvadurai & Mahyari, 1997; Selvadurai et al., 2018). The two-dimensional problem of the internal pressurization of a plane crack located in a poroelastic medium of infinite extent was examined by Detournay and Cheng (1991) where two types of boundary conditions are examined: (i) in the first category of modelling, the fluid pressure at the crack boundary is prescribed as a Heaviside step function of time and the effective stress at the crack surfaces are set to zero, and (ii) in the second category of modelling, the pore fluid pressures on the surfaces of the crack are set to zero and the effective stresses on the crack surfaces are prescribed as Heaviside step functions of time with the same magnitude as the pore fluid pressure in (i). The objective of the current paper is to apply the formal theory of Biot poroelasticity (Biot, 1941, 1956) to examine the mechanics of cracks in a fluid-saturated poroelastic halfspace region. The engineering issues associated with the geosciences and geoengineering activities involve the application of pressures to the fluid-saturated poroelastic geologic formation. The first of these addresses the question related to the pressures that can induce hydraulic fracture of the geologic formations. In some applications, the generation of hydraulic fracture is desirable and in some applications the generation of new hydraulic fractures needs to be prevented. The first of the problems examined in the study addresses the issue where fluid is injected to a location in an initially intact geologic medium. When the injection pressures create an effective stress state that can satisfy a plausible failure criterion the generation of a fracture will result. Once a fracture is nucleated, its propagation is dynamic and will reach a stable configuration; where the geologic medium now contains a crack, whose extension is controlled by the mechanics at the tip of a pressurized crack. The study of the mechanics of cracks in a geologic medium during fluid injection is intimately tied to the in situ stress state. There are no criteria that can be applied a priori to determine which cracks can be initiated in a shallow environment and which can occur at significant depth. In current resource extraction exercises, for example, the depths of location of the resource can exceed 8 km (Selvadurai et al., 2018) and the in situ stress state can be a significant factor in either suppressing fracture extension or altering the orientation of a fracture created by fluid injection. As an example, consider the axisymmetric problem of a penny-shaped crack that is located in a linearly elastic solid under a geostatic stress state where the plane of the penny-shaped crack is subjected to the far field *compressive normal stress* σ_V. Considering the solution to the penny-shaped crack problem (Sneddon, 1946, 1965) the Mode I stress intensity factor at the crack tip is $K_{\mathrm{I}}^{\sigma_V} = (2\sigma_V\sqrt{a}/\pi)$, where a is the radius of the penny-shaped crack. If the applied far field stress is compressive, such a stress state *cannot* result in the extension of the penny-shaped crack in a self similar fashion. The negative stress intensity factor resulting from the far field *compressive stress state* will not promote crack growth. Consider the problem where the penny-shaped crack is located in an unstressed infinite domain and subjected to an internal pressure p_0; the Mode I stress intensity factor is $K_{\mathrm{I}}^{p_0} = (2p_0\sqrt{a}/\pi)$. Let us assume a primitive crack extension criterion, which states that the crack will extend only when in the extensional mode and the resultant stress intensity factor reaches the *critical stress intensity factor in tension*, K_{I}^{C}. Alternatively, an internal pressure $p_0 \geq (\pi K_{\mathrm{I}}^{C}/2\sqrt{a}) + \sigma_V$ will be needed to create an extension of the crack. We can also consider the mechanics of a penny-shaped crack in an infinite elastic medium in the presence of a compressive axial stress σ_V normal to the plane of the crack and a radial stress field σ_R in the plane of the crack. In this case, the internal pressure required to generate an extension of the penny-shaped crack is still $p_0 \geq (\pi K_{\mathrm{I}}^{C}/2\sqrt{a}) + \sigma_V$. The influence of σ_R will not materialize for the case where the penny-shaped crack is located in an infinite space but will influence the generation of an additional stress intensity factor when the penny-shaped crack is located in a halfspace region. The mechanics of penny-shaped cracks in initially stressed media under compression have been considered by Selvadurai (1980) for the problem of an infinite space and by Guz and Nazarenko (1985) for a halfspace region (see also Guz et al., 2020). Therefore, in geomechanics in particular, the influence of the geostatic stress state is an important consideration in the ability to promote growth of existing cracks. The illustration considers only a highly simplified case; in reality the geostatic stress state in a domain can be influenced by several factors, including geodynamic processes, thermal effects and groundwater level fluctuations. The formulation of fracture problems for poroelastic media in an all-encompassing way is not a realistic possibility. Furthermore, the prediction of the orientation of fractures in geomaterials can also be influenced by heterogeneities, defects and preferred orientations with weak fracture toughness characteristics induced by depositional effects. Theoretical and practical experience related to hydraulic fracturing indicates that, in general, in situ fractures will be initiated in orientations normal to the direction of the minimum in situ geostatic principal stress. Since, in general, $\sigma_V > \sigma_R$, unless there is inherent fracture toughness anisotropy, fractures are most likely to be initiated along a vertical plane. This concept has been adopted in the generation of periodic fractures that can emanate from pressurizations induced along directionally drilled and horizontally aligned boreholes (Aadnoy & Looyeh, 2019; Bradley, 1979; Cui et al., 1999; Hossain et al., 2000; Huang et al., 2012; Zhang, 2013). Predicting the orientation of fractures that can emanate from pressurized boreholes that are inclined is a more complicated task. The conventional notions of a planar fracture will not be applicable, and the fractures will develop in a favorable three-dimensional orientation that will not be amenable to convenient mathematical formulation and solution, particularly in the context of the theory of poroelasticity. The objective of this paper is to examine certain canonical problems that can be useful for the calibration of computational approaches to modelling the mechanics of stable fractures in poroelastic media. Of necessity, the modelling is restricted to plausible axisymmetric poroelasticity that is mathematically well-posed and analytically manageable. The examples will deal with the topic of axisymmetric fracture initiation during injection of a fluid into a planar circular region within a poroelastic halfspace domain. The work evaluates the time-dependent surface displacement signatures when controlled, stable, axisymmetric, planar, circular fractures are generated through crack extension during the application of injection pressures. This study will examine the time-dependent

responses of a defect-free poroelastic halfspace and use the solution to compare the response of a poroelastic halfspace containing a pressurized penny-shaped crack. The comparison of time-dependent surface heave can be viewed as a signature of the extent of internal cracking, albeit in an axisymmetric fashion. The study also provides the internal pressurization criteria that can promote the extension of the penny-shaped crack in a self-similar fashion. The extension of the work to include the presence of an impermeable caprock layer is relegated to future work. The contribution of the study to the development of a rigorous investigation of the pressurized penny-shaped crack in a poroelastic halfspace is regarded as a useful bench-mark problem.

2. Governing equations

The poromechanics problems that will be analyzed in this study are formulated within the framework of Biot's classical theory of poroelasticity (Biot, 1941, 1956), where the skeletal deformations are characterized by Hookean isotropic elasticity and the incompressible fluid flow within the pore space is governed by Darcy's law. The classical poroelasticity model or the thermo-poroelasticty model, where the intact porous skeleton exhibits linear elastic behaviour in the small strain range, is certainly restrictive but serves as a suitable approach for examining the coupled responses of many fluid-saturated rocks (Cheng et al., 1993; Selvadurai and Suvorov, 2017). The governing equations are summarized for completeness: the constitutive relations describing isothermal poroelasticity in terms of the total stress tensor $\boldsymbol{\sigma}$ and the pore fluid pressure p are given by (see e.g., Cheng, 2016; Rice & Cleary, 1976)

$$\boldsymbol{\sigma}(r,z,t) = \frac{2G\nu}{(1-2\nu)}\mathrm{tr}\boldsymbol{\varepsilon}(r,z,t)\,\mathbf{I} + 2G\,\boldsymbol{\varepsilon}(r,z,t) - \alpha p(r,z,t)\mathbf{I} \tag{1}$$

In (1), $\boldsymbol{\varepsilon}$ is the infinitesimal strain tensor; $\mathbf{I}$ is the identity matrix; G and ν are, respectively, the linear elastic shear modulus (units Force/Length^2) and the Poisson's ratio of the skeleton. It should also be noted that (1) does not assume the classical Terzaghi (1925) relationship for effective stresses. Improvements to this effective stress law are included in the general theory of poroelasticity developed by Biot (1941), which introduces the Biot coefficient that modifies the pore pressure term in (1). For elastic skeletal behaviour, the Biot coefficient depends on the compressibility of the porous skeleton and the compressibility of the solid material composing the porous skeleton (Biot, 1941; Cheng, 2016; Selvadurai, 2019b). The extension of the classical theory of poroelasticity to include elasto-plastic behaviour of the porous skeleton has been considered by several investigators (Pariseau, 1999; Selvadurai & Suvorov, 2012, 2014; Suvorov & Selvadurai, 2019) and either the material composition or the three-dimensional stress state should contribute to the development of elasto-plasticity. In this case, the Biot coefficient for elasto-plastic behaviour of the porous skeleton can be distinctly different from the purely elastic case. In the absence of body forces, the quasi-static equations of equilibrium in the poroelastic medium can be written as

$$\nabla.\boldsymbol{\sigma} = \mathbf{0}. \tag{2}$$

The fluid is assumed to be incompressible and fluid flow in the porous medium is assumed to be governed by Darcy's law. For a hydraulically isotropic poroelastic medium, Darcy's law takes the form

$$\mathbf{v}^f - \mathbf{v}^s = -\frac{k}{\mu}\gamma_f\,\nabla p, \tag{3}$$

where $\mathbf{v}^f$ is the velocity of the fluid, $\mathbf{v}^s$ is the velocity of the porous skeleton, k is the coefficient of permeability (units Length/Time), μ is the dynamic viscosity of the fluid, and γ_f is its specific weight (units Force/Length^3).

Assuming that the velocity of the porous skeleton is considerably smaller than that of the permeating fluid, the continuity equation associated with quasi-static fluid flow can be written as:

$$\frac{\partial\rho}{\partial t} + \nabla.(\rho\,\mathbf{v}^f) = 0. \tag{4}$$

Expositions of the governing equations and the development of stress function-based representations for their solution are given by several authors and references to these can be found in the following (Cheng, 2016; Kim & Selvadurai, 2015; McNamee & Gibson, 1960a;1960b; Rice & Cleary, 1976; Samea & Selvadurai, 2020; Selvadurai, 2013; Yue and Selvadurai, 1995). For axisymmetric problems formulated with reference to a cylindrical polar coordinate system, these equations can be written in terms of the skeletal displacements $u_r(r,z,t)$ and $u_z(r,z,t)$, respectively in the radial and axial directions, and the pore fluid pressure $p(r,z,t)$ as follows:

$$\left(\nabla^2 u_r - \frac{u_r}{r^2}\right) - (2\eta-1)\frac{\partial\Theta}{\partial r} = \frac{\alpha}{G}\frac{\partial p}{\partial r}, \tag{5}$$

$$\nabla^2 u_z - (2\eta-1)\frac{\partial\Theta}{\partial z} = \frac{\alpha}{G}\frac{\partial p}{\partial z}, \tag{6}$$

$$\beta\frac{\partial p}{\partial t} - \gamma\frac{\partial\Theta}{\partial t} = c\nabla^2 p, \tag{7}$$

where

$$\alpha = \frac{3(\nu_u - \nu)}{B(1-2\nu)(1+\nu_u)} \quad ; \quad \beta = \frac{(1-2\nu_u)(1-\nu)}{(1-2\nu)(1-\nu_u)} \quad ; \quad \gamma = \frac{2GB(1-\nu)(1+\nu_u)}{3(1-2\nu)(1-\nu_u)}$$
$$c = \frac{2GB^2(1-\nu)(1+\nu_u)^2 k}{9(\nu_u-\nu)(1-\nu_u)\gamma_f} = \frac{k\mu}{S_s\gamma_f} \quad ; \quad \eta = \frac{(1-\nu)}{(1-2\nu)}. \tag{8}$$

In these equations, ν_u is the undrained Poisson's ratio, α is the Biot Coefficient, S_s is the storage coefficient, and B is the Skempton's pore pressure parameter defined as

$$B = \frac{C_m - C_s}{C_m - C_s + n\left(C_f - C_s\right)}. \tag{9}$$

where C_m is the compressibility of the porous skeleton; C_s is the compressibility of the skeletal material; C_f is the compressibility of the pore fluid and n is the porosity. The diffusivity coefficient, c, controls the diffusion speed and is a combined property of the hydraulic conductivity, porosity and the compressibility of the solid skeleton as well as the pore fluid (Cheng et al., 1993).

The constitutive parameters have to satisfy certain thermodynamic constraints to ensure positive definiteness of the strain energy potential; these constraints can be expressed in the form $0 \le B \le 1$; $G > 0$; $-1 \le \nu < \nu_u \le 1/2$. Alternative, but equivalent, descriptions are given by Rice and Cleary (1976) and further references can be found in Verruijt (2015), Selvadurai (2013) and Wang (2000).

We also note that Θ and ∇^2 are the volumetric strain and the axisymmetric form of the Laplace's operator given by:

$$\Theta = \frac{\partial u_r}{\partial r} + \frac{u_r}{r} + \frac{\partial u_z}{\partial z}, \tag{10}$$

$$\nabla^2 = \frac{\partial^2}{\partial r^2} + \frac{1}{r}\frac{\partial}{\partial r} + \frac{\partial^2}{\partial z^2}. \tag{11}$$

The solution of the partial differential equations (5)-(7) can be approached in a variety of ways and these have been documented in the literature (McNamee & Gibson, 1960a; Rajapakse & Senjuntichai, 1993; De Josselin de Jong, 1957; Selvadurai, 2007). We adopt the approach proposed in McNamee and Gibson (1960a, 1960b), where the solution to the governing coupled partial differential equations (5)-(7) can be represented in terms of two scalar functions $S(r,z,t)$ and $E(r,z,t)$, which satisfy the coupled partial differential equations

$$\nabla^2 S = 0, \tag{12}$$

$$c\nabla^4 E = \left(\beta + \frac{\alpha\gamma}{2G\eta}\right)\nabla^2\frac{\partial E}{\partial t} - \frac{\beta}{\eta}\frac{\partial^2 S}{\partial z \partial t}. \tag{13}$$

The completeness of these representations has not been proved, but the uniqueness of the initial boundary value problem governing quasi-static poroelasticity problems have been discussed by Altay and Dökmeci (1998). The displacements, total stresses and pore fluid pressure can be uniquely represented in terms of $S(r,z,t)$ and $E(r,z,t)$ as follows:

$$u_z = -\frac{\partial E}{\partial z} + z\frac{\partial S}{\partial z} - S, \qquad u_r = -\frac{\partial E}{\partial r} + z\frac{\partial S}{\partial r}, \tag{14}$$

$$p = \frac{2G}{\alpha}\left(\frac{\partial S}{\partial z} - \eta\,\Theta\right), \qquad \Theta = \nabla^2 E, \tag{15}$$

$$\frac{\sigma_{rr}}{2G} = \left(\frac{\partial^2}{\partial r^2} - \nabla^2\right)E - z\frac{\partial^2 S}{\partial r^2} + \frac{\partial S}{\partial z}, \qquad \frac{\sigma_{\theta\theta}}{2G} = \left(\frac{1}{r}\frac{\partial^2}{\partial r} - \nabla^2\right)E - \frac{z}{r}\frac{\partial S}{\partial r} + \frac{\partial S}{\partial z},$$
$$\frac{\sigma_{zz}}{2G} = \left(\frac{\partial^2}{\partial z^2} - \nabla^2\right)E - z\frac{\partial^2 S}{\partial z^2} + \frac{\partial S}{\partial z}, \qquad \frac{\sigma_{rz}}{2G} = \frac{\partial^2 E}{\partial r \partial z} - z\frac{\partial^2 S}{\partial r \partial z}. \tag{16}$$

The accuracy of the representations (14)-(16) in terms of $S(r,z,t)$ and $E(r,z,t)$ can be verified by back-substitution into the Eqs. (5)–(7). In an analytical approach for the solution of the time-dependent axisymmetric poroelasticity problem, the developments follow integral transform techniques. Laplace and zeroth-order Hankel transforms are used to eliminate, respectively, time-dependency and dependency on the radial coordinate r: i.e.

$$\bar{F}^m(\xi,z,t) = \int_0^\infty r J_m(\xi r) F(r,z,t)\,dr, \tag{17}$$

$$\tilde{F}(\xi,z,s) = \frac{1}{2\pi i}\int_0^\infty e^{-st} F(\xi,z,t)\,dt, \tag{18}$$

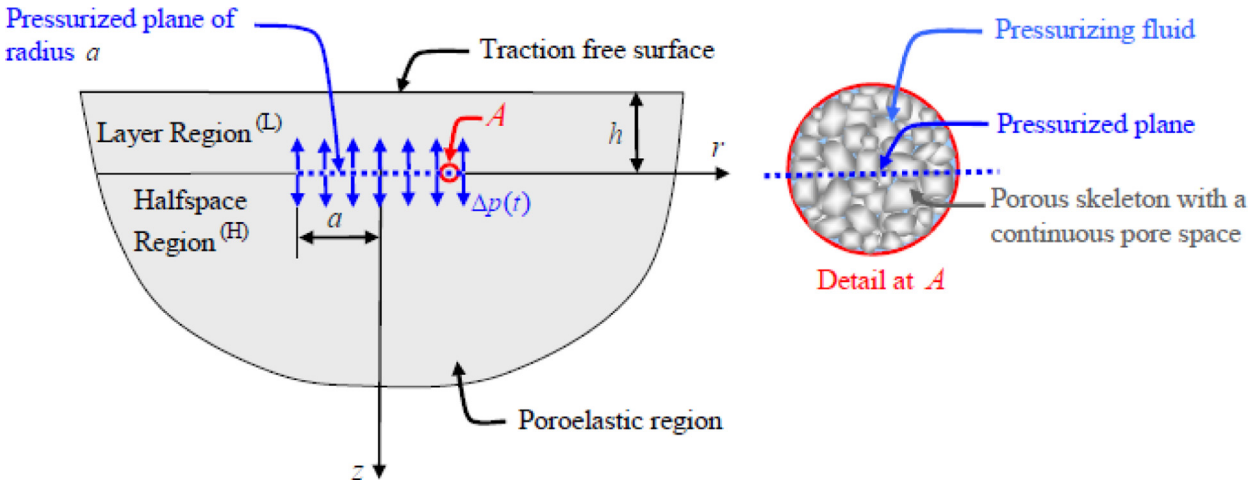

Fig. 1. Internal pressurization of a poroelastic halfspace over a circular region $[\Delta p(t) = p^{(L)}(r,0,t) - p^{(H)}(r,0,t) = p_0 \mathrm{H}(t)\ ;\ 0 \le r < a\ ;\ \forall t > 0]$.

where $(\bar{\ })^m$ refers to the mth-order Hankel transform, $(\tilde{\ })$ refers to the Laplace transform of a particular function and J_m is the Bessel function of the first kind and order m. After successive applications of Laplace and zeroth-order Hankel transforms, the governing PDEs (12) and (13) can be reduced to the following ODEs for the transformed variables $\tilde{\bar{S}}(\xi, z, s)$ and $\tilde{\bar{E}}(\xi, z, s)$:

$$\left(\frac{d^2}{dz^2} - \xi^2\right)\tilde{\bar{S}}(\xi, z, s) = 0, \tag{19}$$

$$\left(\frac{d^2}{dz^2} - \xi^2\right)\left\{\frac{d^2}{dz^2} - \left[\xi^2 + \frac{s}{c}\left(\beta + \frac{\alpha\gamma}{2G\eta}\right)\right]\right\}\tilde{\bar{E}}(\xi, z, s) = -\frac{\beta s}{\eta c}\frac{d}{dz}\tilde{\bar{S}}(\xi, z, s). \tag{20}$$

This approach is found to be the most convenient and has been applied to solve a variety of initial mixed boundary value problems related to contact mechanics in poroelasticity. For a comprehensive account of such problems, readers are referred to a recent study by Selvadurai and Samea (2020).

3. Skeletal stress development due to fluid injection over a circular region

The problem of fluid injection along line sources into a poroelastic halfspace region, with prescribed poro-mechanical properties, geomechanical skeletal strength characteristics, and overlain by an impermeable elastic caprock, was presented by Kim and Selvadurai (2015). In their study, the fluid injection rates that can promote the development of fracture within the storage formation was examined. This category of problems is of interest to the study of the injection of fluidized greenhouse gases into storage formations. Even though the analysis was based on isothermal poromechanics, the findings can contribute to the modelling of the time-dependent influences of poromechanics and supplements purely elastic modelling similar to the studies given in Selvadurai (2009, 2012). In the study by Selvadurai and Kim (2016), attention was focused on the injection of fluids into a similar storage setting and the fluid injection was applied over a circular region that preserved axisymmetric conditions. Also, the influence of the poroelastic properties of the caprock layer was an added modification. These studies provided a methodology to control the initiation of fracture of the storage formation; the creation of such defects would render the storage formation of little value since the created fractures could compromise the storage potential. Furthermore, when a free boundary is encountered, any created fractures would have the tendency to extend to the free surface, thereby providing a pathway for the leakage of the injected greenhouse gases. In the current study, the potential for creating a hydraulic fracture is first examined by investigating the poroelastic effective stresses created in an *intact* poroelastic storage halfspace region and the influences of the caprock layer are excluded. In fluid injection exercises, the rate of injection is usually achieved in a progressive fashion. In this modelling the fluid pressure of magnitude p_0 is instantaneously applied as a Heaviside step function of time and the fluid enters a halfspace at a plane circular region of radius a located at a depth h from the surface of the halfspace region (Fig. 1).

For the formulation of the mixed initial boundary value problem related to the fluid injection, it is convenient to designate (i) a layer region $^{(L)}$, where $0 \le r < \infty$ and $-h \le z \le 0$, and (ii) a reduced halfspace region $^{(H)}$, where $0 \le r < \infty$ and $0 \le z < \infty$.

(i) On the surface of the layer region, we have

$$\sigma_{zz}^{(\mathrm{L})}(r,-h,t)=\sigma_{rz}^{(\mathrm{L})}(r,-h,t)=0 \quad ; \quad 0\le r<\infty \quad ; \quad \forall t\ge 0 \tag{21}$$

$$p^{(\mathrm{L})}(r,-h,t)=0 \quad ; \quad 0\le r<\infty \quad ; \quad \forall t\ge 0 \tag{22}$$

(ii) When considering the interface between the layer region and the halfspace region, it is convenient to consider, for future use, the continuity conditions associated with the region *exterior* to the injection zone $a\le r<\infty$; $z=0$ and the *interior* region where the injection takes place. The continuity conditions at the *exterior* region located at the plane $z=0$ can be written as

$$u_r^{(\mathrm{L})}(r,0,t)-u_r^{(\mathrm{H})}(r,0,t)=0 \quad ; \quad a\le r<\infty \quad ; \quad \forall t\ge 0 \tag{23}$$

$$u_z^{(\mathrm{L})}(r,0,t)-u_z^{(\mathrm{H})}(r,0,t)=0 \quad ; \quad a\le r<\infty; \quad \forall t\ge 0 \tag{24}$$

$$\sigma_{zz}^{'(\mathrm{L})}(r,0,t)-\sigma_{zz}^{'(\mathrm{H})}(r,0,t)=0 \quad ; \quad a\le r<\infty \quad ; \quad \forall t\ge 0 \tag{25}$$

$$\sigma_{rz}^{(\mathrm{L})}(r,0,t)-\sigma_{rz}^{(\mathrm{H})}(r,0,t)=0 \quad ; \quad a\le r<\infty \quad ; \quad \forall t\ge 0 \tag{26}$$

$$p^{(\mathrm{L})}(r,0,t)-p^{(\mathrm{H})}(r,0,t)=0 \quad ; \quad a\le r<\infty \quad ; \quad \forall t\ge 0 \tag{27}$$

$$\left(\frac{\partial p^{(\mathrm{L})}}{\partial z}\right)_{z=0}-\left(\frac{\partial p^{(\mathrm{H})}}{\partial z}\right)_{z=0}=0 \quad ; \quad a\le r<\infty \quad ; \quad \forall t\ge 0 \tag{28}$$

Considering the *interior* region located at the plane $z=0$, we have

$$u_r^{(\mathrm{L})}(r,0,t)-u_r^{(\mathrm{H})}(r,0,t)=0 \quad ; \quad 0\le r\le a \quad ; \quad \forall t\ge 0 \tag{29}$$

$$u_z^{(\mathrm{L})}(r,0,t)-u_z^{(\mathrm{H})}(r,0,t)=0 \quad ; \quad 0\le r\le a \quad ; \quad \forall t\ge 0 \tag{30}$$

$$\sigma_{zz}^{(\mathrm{L})}(r,0,t)-\sigma_{zz}^{(\mathrm{H})}(r,0,t)=p^{(\mathrm{L})}(r,0,t)-p^{(\mathrm{H})}(r,0,t) \quad ; \quad 0\le r\le a \quad ; \quad \forall t\ge 0 \tag{31}$$

$$\sigma_{rz}^{(\mathrm{L})}(r,0,t)-\sigma_{rz}^{(\mathrm{H})}(r,0,t)=0 \quad ; \quad 0\le r\le a \quad ; \quad \forall t\ge 0 \tag{32}$$

$$p^{(\mathrm{L})}(r,0,t)-p^{(\mathrm{H})}(r,0,t)=p_0\mathrm{H}(t) \quad ; \quad 0\le r<a; \quad \forall t\ge 0 \tag{33}$$

$$\left(\frac{\partial p^{(\mathrm{L})}}{\partial z}\right)_{z=0}-\left(\frac{\partial p^{(\mathrm{H})}}{\partial z}\right)_{z=0}=0 \quad ; \quad 0\le r<a \quad ; \quad \forall t\ge 0 \tag{34}$$

where t is the lapse time since the crack faces are exposed to the injected fluid, $\mathrm{H}(t)$ is the Heaviside step function of time, and $\sigma'_{ij}\in\sigma_{ij}-\alpha p\delta_{ij}$) is the effective stress. These boundary conditions should also be supplemented by the regularity conditions applicable to both the layer and the halfspace regions.

$$\lim_{|\mathrm{x}|\to\infty}\left\{\sigma^{(i)}(\mathrm{x},\ t),\ \mathrm{u}^{(i)}(\mathrm{x},\ t),\ p^{(i)}(\mathrm{x},\ t)\right\}=0 \quad ; \quad i=\mathrm{L},H \quad ; \quad \forall t\ge 0 \tag{35}$$

For the solution of the transient problem, the initial conditions are prescribed as follows:

$$\left.\begin{array}{l}\mathbf{u}^{(\mathrm{L})}(\mathbf{x},t)=\mathbf{u}^{(\mathrm{H})}(\mathbf{x},t)=0\\ \boldsymbol{\sigma}^{(\mathrm{L})}(\mathbf{x},t)=\boldsymbol{\sigma}^{(\mathrm{H})}(\mathbf{x},t)=0\\ p^{(\mathrm{L})}(\mathbf{x},t)=p^{(\mathrm{H})}(\mathbf{x},t)=0\end{array}\right\} \quad ; \quad t=0 \tag{36}$$

Ensuring that the regularity conditions (35) are satisfied, the solution to the governing ordinary differential Eqs. (19) and (20) for the layer and halfspace regions can be given as

$$\tilde{\tilde{S}}^{(\mathrm{L})}(\xi,z,s)=A_1^{(\mathrm{L})}e^{-\xi z}+B_1^{(\mathrm{L})}e^{\xi z}, \tag{37}$$

$$\tilde{\tilde{E}}^{(\mathrm{L})}(\xi,z,s)=A_2^{(\mathrm{L})}e^{-\xi z}+B_2^{(\mathrm{L})}e^{\xi z}+A_3^{(\mathrm{L})}e^{-\varphi z}+B_3^{(\mathrm{L})}e^{\varphi z}+\Gamma A_1^{(\mathrm{L})}z\,e^{-\xi z}+\Gamma B_1^{(\mathrm{L})}z\,e^{\xi z}, \tag{38}$$

$$\tilde{\bar{S}}^{(\mathrm{H})}(\xi, z, s) = A_1^{(\mathrm{H})} e^{-\xi z}, \tag{39}$$

$$\tilde{\bar{E}}^{(\mathrm{H})}(\xi, z, s) = A_2^{(\mathrm{H})} e^{-\xi z} + A_3^{(\mathrm{H})} e^{-\varphi z} + \Gamma A_1^{(\mathrm{H})} z e^{-\xi z}. \tag{40}$$

In these equations, $A_1^{(\mathrm{L})}$, $B_1^{(L)}$, ..., $A_3^{(\mathrm{H})}$ are arbitrary functions to be determined by imposing boundary conditions (17)-(25). In the above, φ and Γ are defined by the following expressions:

$$\varphi = \sqrt{\xi^2 + \frac{c}{s}\left(\beta + \frac{\alpha\,\gamma}{2G\,\eta}\right)} \qquad ; \qquad \Gamma = \frac{\beta\,G}{2\eta\,\beta\,G + \alpha\,\gamma}. \tag{41}$$

Avoiding details, the initial boundary value problem governing the fluid injection problem defined by (21) to (36) can be solved to obtain the displacements, stresses and pore fluid pressures in the layer and the halfspace regions. Integral expressions for the axial displacements, the stress components and the pore pressure fields are given in Appendix A.

In addition, we consider the in situ geostatic stress state that can be generated by the self weight of the material and the initial pore fluid pressure distribution corresponding to the case where the groundwater level is at the surface of the layer region. For the layer region and the reduced halfspace region, the initial geostatic *effective stress* state is given by

$$\boldsymbol{\sigma}'^{(i)\,GS} = (h+z)(\gamma_s - \gamma_w)\begin{pmatrix} \frac{\nu}{1-\nu} & 0 & 0 \\ 0 & \frac{\nu}{1-\nu} & 0 \\ 0 & 0 & 1 \end{pmatrix} \qquad ; \qquad \begin{matrix} i = \mathrm{L}\ \ (-h \le z \le 0) \\ i = \mathrm{H}\ \ (0 \le z < \infty) \end{matrix} \tag{42}$$

where γ_s is the bulk unit weight of the geomaterial and the superscript ^{GS} refers to the geostatic stress state.

The topic of nucleation of fractures in geomaterials is a complex issue, which is distinct from the extension of existing cracks under applied stresses pioneered by Griffith. The subject of nucleation of cracks or voids in a material needs to consider the creation of new surfaces in an otherwise intact region. This is usually postulated by appeal to an observation based on a theory of failure or energetic considerations. Many such theories have been postulated in the literature (Broek, 1982; Cherepanov, 1979; Hellan, 1985; Lawn & Wilshaw, 1975; Popelar & Kanninen, 1985; Sih, 1991; Sneddon & Lowengrub, 1969; Spencer, 1965) and the problem can be complicated due to the presence of a saturating fluid in the pore space. A plausible approach, particularly in connection with the fluid injection problem, is to examine the initiation of a fracture when the skeletal tensile strength of the material, as interpreted by the effective stresses, is reached. In the case of the axisymmetric fluid injection problem, this would allow axisymmetric conditions to be maintained during the injection process. Other failure criteria such as the Mohr-Coulomb, Tresca, Drucker-Prager, Mogi, Hoek-Brown etc. (Benz & Schwab, 2008; Davis & Selvadurai, 2005; Jiang & Xie, 2011; Rahimi & Nygaard, 2015), can be used to assess the initiation of failure; however, such criteria will invariably lead to inclined orientations of failure planes that are possible but would not be amenable to the analytical treatment of the injection problem. Here, we assume that a stable axisymmetric penny-shaped crack emanating from the center of the injection zone can form in the plane of the injection zone. The dimension of such a crack will depend on the skeletal fracture criteria but, for purposes of simplification of the analytical treatment, we consider the presence of a crack that will coincide with the injection zone. The analysis of this problem is given in Section 4.

In this section we briefly examined the conditions that will promote the nucleation of a crack at an injection zone and how (i) the fluid pressure, (ii) the poroelastic and strength parameters of the rock, (iii) the geostatic stress state, and (iv) the depth of location and the dimensions of the planar injection zone, can influence the initiation of a crack. The variation of effective axial stresses at the plane of injection is given by

$$\sigma_{ij}'^{*}(r, 0, t) = \sigma_{ij}'^{GS}(r, 0) - \left\{\sigma_{ij}(r, 0, t) - \alpha\delta_{ij}p(r, 0, t)\right\} \tag{43}$$

The maximum value of the steady injection rate that initiates the development of failure at the *central location* of the injection zone occurs when the stress state reaches a critical level defined by a proper failure criterion in terms of principle effective stresses.

4. Fluid injection into a created penny-shaped crack located in a poroelastic halfspace

The analysis presented in the previous section demonstrates that when appropriate stress states prevail, the injection of fluids into intact poroelastic geological formations can lead to fracture development. Once a crack is nucleated, the presence of an injection pressure within the nucleated zone will promote the growth of the crack if the criteria for crack extension are satisfied. The propensity for the fracture extension to occur in either a controlled or uncontrolled fashion (Atkinson, 1984; Lawn & Wilshaw, 1975) will depend on the competition between the fracture toughness criteria, the injection pressures of the fracturing fluids and the permeability of the poroelastic medium. If uncontrolled fracture growth takes place, the speed of propagation of the fracture can attain the Rayleigh wave speeds and such dynamic crack extension criteria are recognized as a signature of a process similar to waves generated during earthquake rupture. The studies performed by Atkinson and Craster (1991, 1995) provide excellent accounts of the interplay between the speed of propagation of a crack in a poroelastic medium and the influence of permeability in the alteration of the effective stress intensity factor at a crack tip. A great deal

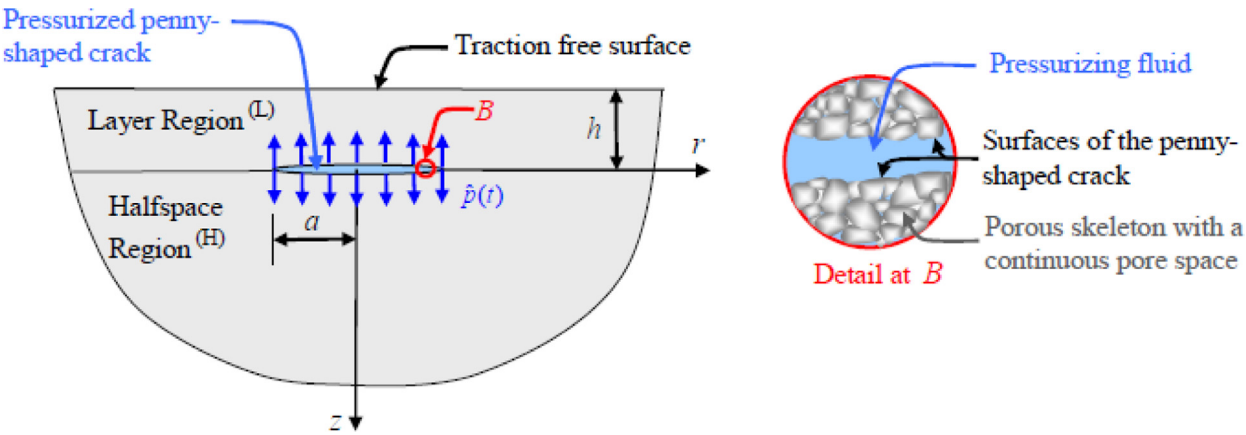

Fig. 2. Internal pressurization of a penny-shaped crack in a poroelastic halfspace [$\hat{p}(t) = p^{(L)}(r,0,t) = p^{(H)}(r,0,t) = p_0 \mathrm{H}(t)\ ;\ 0 \le r < a\ ;\ \forall t > 0$].

of attention has also been given to dynamic crack extension in the context of resource exploration (Jin & Zhong, 2002; Song et al., 2017) by hydraulic fracturing (or the vulgar term, fracking). The consideration of the dynamic crack extension problem in the context of the theory of poroelasticity is important but is not within the scope of this paper.

The analysis presented here focuses on a stable crack that is created within a halfspace region during the fluid injection process. In the case of a crack located within a poroelastic halfspace, the crack tip will contain two stress intensity factors and the initiation of fracture propagation in the skeleton will be of a mixed mode type. This implies that the crack might deviate from a planar form to an axisymmetric three-dimensional configuration, which is not amenable to a purely mathematical formulation. As a plausible approximation, we assume that the extension of the crack will be in a Mode I fashion, thereby generating an axisymmetric penny-shaped crack within the axisymmetric injection zone (Fig. 2). There are several manifestations of the crack generation; these can include (i) a sudden pressure drop in the injection fluids, (ii) the generation of seismic waves and (iii) the displacements of the rock mass that will be observed at the surface of the poroelastic halfspace. The intention here is to develop a poroelastic solution for the case where nucleated cracks extend to the boundary of the injection zone and reach a stable configuration where injection takes place at a constant fluid pressure p_0 (units Force/Length^2), ensuring that a mixed-mode failure criterion is satisfied.

Thus, we focus attention on the solution of a mixed boundary value problem in poroelasticity related to fluid injection, such that the surfaces of the crack are maintained at a constant pressure. The axisymmetric initial mixed boundary value problem for a pressurized penny-shaped crack in a poroelastic halfspace is governed by the following mixed boundary conditions: For the layer region, with a free-draining boundary, we have a similar set of constraints as in (21) and (22).

The pressurization of the penny-shaped crack is carried out over a planar circular zone occupying the region $0 \le r \le a$ at $z = 0$ with a constant pressure p_0 (units Force/Length^2). At the pressurization level, within the crack region, the mathematical formulation of the problem should also satisfy the continuity of displacements, stresses and the fluid flux, i.e.

$$\sigma_{zz}^{(L)}(r,0,t) = \sigma_{zz}^{(H)}(r,0,t) = \sigma\,\mathrm{H}(t) \quad ; \quad 0 < r < a \quad ; \quad \forall t \ge 0 \tag{44}$$

$$\sigma_{rz}^{(L)}(r,0,t) = \sigma_{rz}^{(H)}(r,0,t) = 0 \quad ; \quad 0 < r < a \quad ; \quad \forall t \ge 0 \tag{45}$$

$$p^{(L)}(r,0,t) = p^{(H)}(r,0,t) = p_0\,\mathrm{H}(t) \quad ; \quad 0 < r < a \quad ; \quad \forall t \ge 0 \tag{46}$$

$$\left(\frac{\partial p^{(L)}}{\partial z}\right)_{z=0} = \left(\frac{\partial p^{(H)}}{\partial z}\right)_{z=0} \quad ; \quad 0 \le r < a \quad ; \quad \forall t \ge 0 \tag{47}$$

and the continuity conditions at the *exterior* of the crack region, within the pressurization level, are similar to the boundary conditions (23)-(27).

These boundary conditions should also satisfy the regularity conditions (35) and the initial conditions governing the fluid injection problem (36). Two loading cases can be considered for the choice of σ : Case 1, when both the porous skeleton and the pore fluid take part in the transfer of the applied pressure within the injection region; i.e. $\sigma_{zz}^{(L)}(r,0,t) = \sigma_{zz}^{(H)}(r,0,t) = \sigma\,\mathrm{H}(t) = 0$; and Case 2, when the boundary condition assumes that the effective stress is zero at the injection region and the applied pressure is transferred only through the interstitial fluid, i.e. $\sigma_{zz}^{(L)}(r,0,t) = \sigma_{zz}^{(H)}(r,0,t) = \sigma\,\mathrm{H}(t) = \alpha\,p_0\mathrm{H}(t)$.

4.1. Solution of the initial mixed boundary value problem

Using (37)-(40) together with the transformed expressions for the displacements, stresses and pore fluid pressure (14)-(16), the mixed boundary value problem (23)-(28) and (44)-(47) for both loading cases can be written in the form of three sets of dual integral equations. These equations can be written as:

$$\int_0^\infty \xi^2\left\{\left(\tilde{\vartheta}_{11}+1\right)\tilde{\bar{N}}_1(\xi,s)+\tilde{\vartheta}_{12}\tilde{\bar{N}}_2(\xi,s)+\tilde{\vartheta}_{13}\tilde{\bar{N}}_3(\xi,s)\right\}J_0(\xi r)d\xi=\sigma/s \quad ; \quad r<a \quad ; \quad \forall t\geq 0 \tag{48}$$

$$\int_0^\infty \xi\tilde{\bar{N}}_1(\xi,s)J_0(\xi r)d\xi=0 \quad ; \quad r\geq a \quad ; \quad \forall t\geq 0 \tag{49}$$

$$\int_0^\infty \left\{\tilde{\vartheta}_{21}\tilde{\bar{N}}_1(\xi,s)+\left(\tilde{\vartheta}_{22}+1\right)\tilde{\bar{N}}_2(\xi,s)+\tilde{\vartheta}_{23}\tilde{\bar{N}}_3(\xi,s)\right\}J_0(\xi r)d\xi=p_0/s \quad ; \quad r<a \quad ; \quad \forall t\geq 0 \tag{50}$$

$$\int_0^\infty \xi\tilde{\bar{N}}_2(\xi,s)J_0(\xi r)d\xi=0 \quad ; \quad r\geq a \quad ; \quad \forall t\geq 0 \tag{51}$$

$$\int_0^\infty \xi^2\left\{\tilde{\vartheta}_{31}\tilde{\bar{N}}_1(\xi,s)+\tilde{\vartheta}_{32}\tilde{\bar{N}}_2(\xi,s)+\left(\tilde{\vartheta}_{33}+1\right)\tilde{\bar{N}}_3(\xi,s)\right\}J_1(\xi r)d\xi=0 \quad ; \quad r<a \quad ; \quad \forall t\geq 0 \tag{52}$$

$$\int_0^\infty \xi\tilde{\bar{N}}_3(\xi,s)J_0(\xi r)d\xi=0 \quad ; \quad r\geq a \quad ; \quad \forall t\geq 0 \tag{53}$$

where $\tilde{\bar{N}}_i(\xi,s);\ i=1,\ 2,\ 3$ can admit the following finite Fourier transforms (Copson, 1961; Sneddon, 1951) such that

$$\tilde{\bar{N}}_1(\xi,s)=\frac{1}{\xi}\int_0^a \tilde{\phi}_1(\rho,s)\sin(\xi\rho)\,d\rho, \tag{54}$$

$$\tilde{\bar{N}}_2(\xi,s)=\int_0^a \tilde{\phi}_2(\rho,s)\cos(\xi\rho)\,d\rho, \tag{55}$$

$$\tilde{\bar{N}}_3(\xi,s)=\sqrt{\frac{1}{\xi}}\int_0^a \tilde{\phi}_3(\rho,s)J_{\frac{3}{2}}(\xi\,\rho)\,d\rho. \tag{56}$$

With the aid of the representation (54)-(56), the dual integral Eqs. (48)–(53) can be reduced to the following simultaneous Fredholm integral equations of the second kind:

$$\begin{aligned}\tilde{\phi}_1(r,s)+\int_0^a \tilde{\phi}_1(\rho,s)\tilde{\Omega}_{11}(r,\rho,s)\,d\rho+\int_0^a \tilde{\phi}_2(\rho,s)\tilde{\Omega}_{12}(r,\rho,s)\,d\rho\\ +\int_0^a \tilde{\phi}_3(\rho,s)\tilde{\Omega}_{13}(r,\rho,s)\,d\rho=2\sigma\,r/\pi s \quad ; \quad r<a\end{aligned} \tag{57}$$

$$\begin{aligned}\int_0^a \tilde{\phi}_1(\rho,s)\tilde{\Omega}_{21}(r,\rho,s)\,d\rho+\tilde{\phi}_2(r,s)+\int_0^a \tilde{\phi}_2(\rho,s)\tilde{\Omega}_{22}(r,\rho,s)\,d\rho\\ +\int_0^a \tilde{\phi}_3(\rho,s)\tilde{\Omega}_{23}(r,\rho,s)\,d\rho=2p_0/\pi s \quad ; \quad r<a\end{aligned} \tag{58}$$

$$\begin{aligned}\int_0^a \tilde{\phi}_1(\rho,s)\tilde{\Omega}_{31}(r,\rho,s)\,d\rho+\int_0^a \tilde{\phi}_2(\rho,s)\tilde{\Omega}_{32}(r,\rho,s)\,d\rho+\tilde{\phi}_3(r,s)\\ +\int_0^a \tilde{\phi}_3(\rho,s)\tilde{\Omega}_{33}(r,\rho,s)\,d\rho=0 \quad ; \quad r<a\end{aligned} \tag{59}$$

The expressions for the kernel functions $\tilde{\Omega}_{ij}(r,\rho,s)\ ;\ i,j=1,\ 2,\ 3$ are given in Appendix B.

The solution of the set of Fredholm integral Eqs. (57)–(59) for the unknown functions $\tilde{\phi}_1(r,s)$, $\tilde{\phi}_2(r,s)$, and $\tilde{\phi}_3(r,s)$ can be used to evaluate the fracture response and the variations in displacements, stresses and pore fluid pressure within the medium. A result of importance to geomechanical applications is the evaluation of both Mode I and Mode II stress intensity factors at the crack tip for any of the loading cases:

$$K_{\mathrm{I}}^{(m)}=\lim_{r\to a^+}\left\{\sqrt{2(r-a)}\sigma_{zz}^{(\mathrm{L})}(r,0,t)\right\}=-\frac{\tilde{\phi}_1(a,s)}{\sqrt{a}} \quad ; \quad m=1,\ 2 \tag{60}$$

$$K_{\mathrm{II}}^{(m)}=\lim_{r\to a^+}\left\{\sqrt{2(r-a)}\sigma_{rz}^{(\mathrm{L})}(r,0,t)\right\}=-\sqrt{\frac{2}{\pi}}\frac{\tilde{\phi}_3(a,s)}{a} \quad ; \quad m=1,\ 2 \tag{61}$$

The possibility of the extension of the penny-shaped crack can be checked by comparing the time-dependent skeletal stress intensity factors at the crack tip with a mixed-mode brittle fracture criterion.

The crack volume for any of the loading cases can be calculated by integrating the crack opening displacements along the crack face $(0, a)$:

$$\tilde{V}_c^{(m)}(s) = 2\pi \int_0^a r\left[\tilde{u}_z^{(\mathrm{L})}(r,0,s) + \tilde{u}_z^{(\mathrm{H})}(r,0,s)\right]dr \quad ; \quad m = 1,\ 2 \tag{62}$$

4.2. Solution of the system of Fredholm integral Eqs

The sets of coupled Fredholm integral Eqs. of the second kind (57)-(59) governing fluid injection into a penny shaped crack in a poroelastic halfspace are not amenable to exact solutions. To achieve the Laplace transform inversion, the interval $(0,\ a]$ is divided into N equal sub-intervals with their endpoints located at $r_i = (i-1)a/N$; $(i = 1,\ 2,\ 3,\ ...,\ N+1)$, and the collocation points defined at $p_i = (r_i - r_{i+1})/2$; $(i = 1,\ 2,\ 3,\ ...,\ N)$. The Fredholm integral Eqs. in (57)-(59) can then be written in the form of a system of algebraic Eqs.:

$$\sum_{i,j}^{N}\left[\tilde{\mathbf{H}}^{ij}\right]\left\{\tilde{\mathbf{P}}^{i}\right\} = \left\{\tilde{\mathbf{B}}^{j}\right\}, \tag{63}$$

where the components of the matrices $[\tilde{\mathbf{H}}^{ij}]$, $\{\tilde{\mathbf{P}}^{i}\}$, and $\{\tilde{\mathbf{B}}^{i}\}$ are defined as

$$\left[\tilde{\mathbf{H}}_{pq}^{ij}\right] = \begin{cases} \delta_{ij} + \dfrac{1}{N}\tilde{\Omega}_{pq}(r_i, r_j) & ; \quad i = j = 1,\ \ldots,\ N \ ; \ p = q = 1-3 \\ \dfrac{1}{N}\tilde{\Omega}_{pq}(r_i, r_j) & ; \quad i = j = 1,\ \ldots,\ N \ ; \ p \neq q = 1-3 \\ \dfrac{1}{N}\tilde{\Omega}_{pq}(r_i, r_j) & ; \quad i \neq j = 1,\ \ldots,\ N \end{cases} \tag{64}$$

$$\left\{\tilde{\mathbf{P}}^{j}\right\} = \left\{\tilde{\phi}_1(r_i), \tilde{\phi}_2(r_i), \tilde{\phi}_3(r_i)\right\}^T \quad ; \quad i, j = 1,\ \ldots,\ N \tag{65}$$

$$\left\{\tilde{\mathbf{B}}_p^{i}\right\} = \begin{cases} 2\sigma r_i/\pi s & ; \quad p = 1 \ ; \quad i = 1,\ \ldots,\ N \\ 2p_0/\pi s & ; \quad p = 2 \ ; \quad i = 1,\ \ldots,\ N \\ 0 & ; \quad p = 3 \ ; \quad i = 1,\ \ldots,\ N \end{cases} \tag{66}$$

in which δ_{ij} is the Kronecker's delta function.

From the solution of the set of equations in (63) for $\tilde{\phi}_1(r_i, s)$, $\tilde{\phi}_2(r_i, s)$, and $\tilde{\phi}_3(r_i, s)$, the normalized Mode I and Mode II stress intensity factor in the discretized form can be given as

$$\tilde{K}_{\mathrm{I}}^{(m)}(s) = -\frac{a}{p_0}\tilde{\phi}_1(r_N, s) \quad ; \quad m = 1, 2 \tag{67}$$

$$\tilde{K}_{\mathrm{II}}^{(m)}(s) = -\sqrt{\frac{2}{\pi}}\frac{a}{p_0}\tilde{\phi}_3(r_N, s) \quad ; \quad m = 1, 2 \tag{68}$$

Solutions were found for the Laplace transforms of the unknown functions $\tilde{\phi}_1(r, s)$, $\tilde{\phi}_2(r, s)$, and $\tilde{\phi}_3(r, s)$. To recover the time-dependent functions $\phi_1(r, t)$, $\phi_2(r, t)$, and $\phi_3(r, t)$, the transforms should be inverted using an appropriate numerical Laplace inversion technique. Here, we use the Laplace inversion technique proposed by Schapery (1962). Alternative techniques for inversion of Laplace transforms are given by Cheng et al. (1994), and Cohen (2007).

5. Computational modelling

One of the objectives of this article is to calibrate the accuracy of computational schemes that can be applied to more complex problems relevant to the geological sequestration of greenhouse gases, and extraction of geothermal and oil and gas resources in order to examine the extent to which computational codes can provide reliable results. The computational solutions to the injection problems discussed earlier were obtained using the COMSOL© multiphysics finite element platform. Figs. 3 and 4, respectively show the geometry of the model and the boundary conditions implemented in the FE code to simulate the instantaneous injection of a fluid applied at a constant pressure into a circular region and a penny-shaped crack within a poroelastic medium. An axisymmetric model was developed due to the symmetry of the problem about the z-axis. No infinite elements were employed in the model, but the outer boundaries of the domain are located sufficiently remote from the injection zone to minimize the influence of finite boundaries and ensure that far-field boundary conditions are imposed [the discretized domain includes the region bounded between $r \in (0,\ R = 100\,a)$ and $z \in (0, D = 100a + h)$]. This approach was successfully used in previous investigations involving contact problems for poroelastic media (Samea & Selvadurai, 2020; Selvadurai & Samea, 2020). At the outer boundary of the domain $z = 0$, the pore fluid pressure is zero and

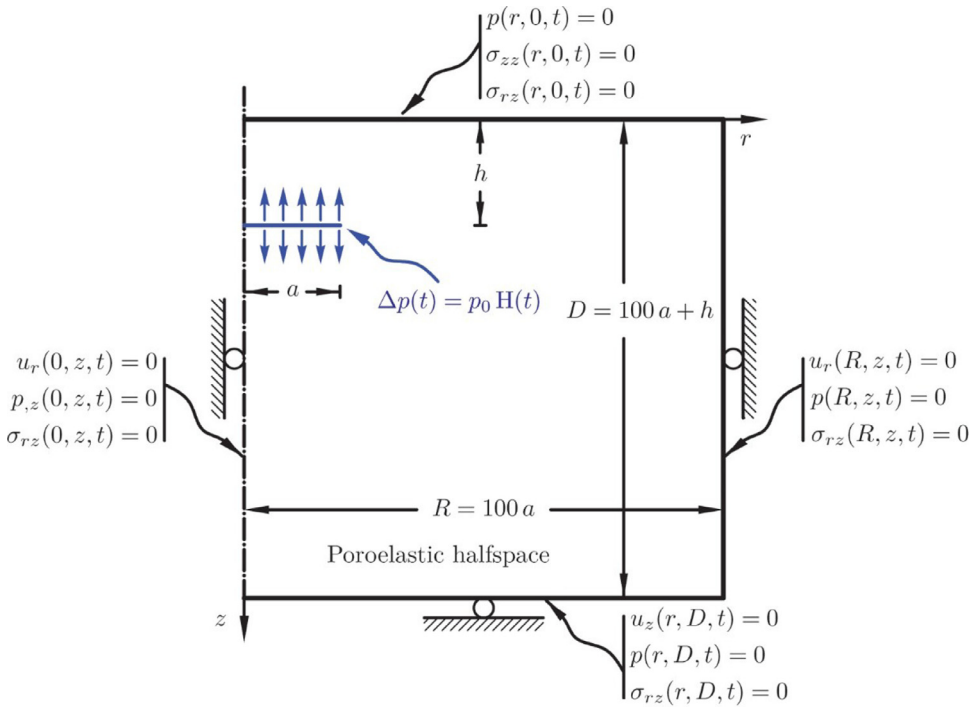

Fig. 3. The geometry of the domain and the boundary conditions implemented in the FE simulation for fluid injection into a planar circular zone within a poroelastic medium [$\Delta p(t)=p^{(\mathrm{L})}(r,0,t)-p^{(\mathrm{H})}(r,0,t)=p_0\mathrm{H}(t)\,;\ 0\le r<a\,;\ \forall t>0$].

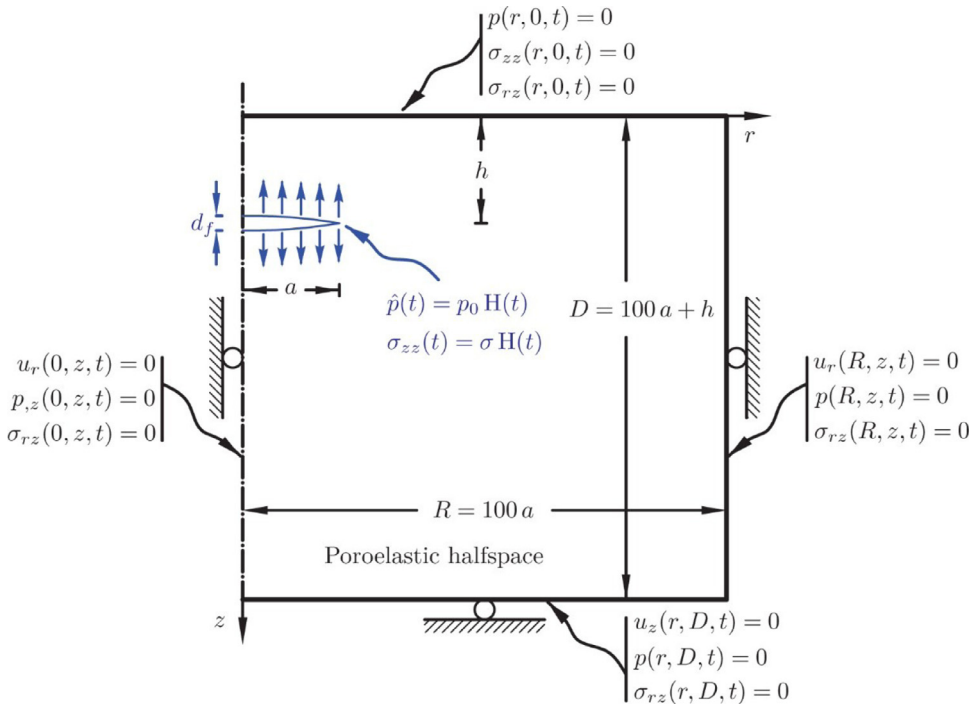

Fig. 4. The geometry of the domain and the boundary conditions implemented in the FE simulation for fluid injection into a penny-shaped crack within a poroelastic medium [$\hat{p}(t)=p^{(\mathrm{L})}(r,0,t)=p^{(\mathrm{H})}(r,0,t)=p_0\mathrm{H}(t)\,;\ 0\le r<a\,;\ \forall t>0$].

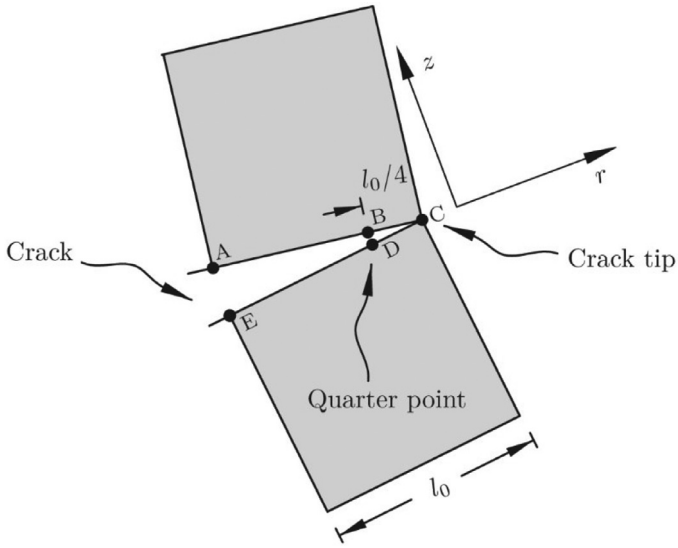

Fig. 5. Crack tip geometry.

a free boundary condition is imposed. A graded mesh discretization was adopted throughout the model with extra mesh refinements to ensure mesh independence of the computational results. The mesh for the problem described in Fig. 3, consists of extra-fine isoparametric quadratic rectangular elements with two in-plane degrees of freedom at each node and a maximum element growth rate of 1.1.

The geometry of the crack was created by means of linear segments having a maximum aperture size of $d_f/a = 2 \times 10^{-5}$. For Case 1 loading, at $z = h$ a constant pressure, p_0, was applied on both faces of the crack. For Case 2, a boundary stress equal to αp_0 was also added on the crack face at $z = h$. At the outer boundary $z = 0$, the pore fluid pressure is set to zero and a free boundary condition is imposed. For the problem described in Fig. 4, isoparametric elements with a quartic shape order discretization were introduced to capture the crack tip behavior and the singular pore pressure and stress fields present at the discontinuous boundaries of the geometry. Of central concern has been the development of techniques to quantify the crack tip stress intensity factors. These techniques, in general, fall into two main categories: energy techniques, which calculate the stress intensity factors (SIFs) through a correlation with the energy release rate. Techniques such as J-integral (Rice, 1968), Virtual Crack Extension (VCE) (Parks, 1974) and Virtual Crack Closure (VCC) (Rybicki & Kanninen, 1977) are examples of methods that are proposed under the Linear Elastic Fracture Mechanics (LEFM) assumption. The alternative is the use of direct approaches, such as stress or displacement correlation/extrapolation techniques (Chan et al., 1970; Shih et al., 1976), which take advantage of the relationship between SIFs and the stress or displacement fields of the points adjacent to the crack tip. We adopt the Displacement Correlation (DC) scheme introduced by Barsoum (1976) and Shih et al. (1976) where both crack opening and shearing stress intensity factors can be evaluated in terms of the nodal displacements of the crack tip element at opposite sides (Fig. 5), i.e.:

$$K_{\mathrm{I}} = \frac{G}{4(1-\nu)}\sqrt{\frac{2\pi}{l_0}}[4(u_z(B) - u_z(D)) + u_z(E) - u_z(A)], \tag{69}$$

$$K_{\mathrm{II}} = \frac{G}{4(1-\nu)}\sqrt{\frac{2\pi}{l_0}}[4(u_r(B) - u_r(D)) + u_r(E) - u_r(A)], \tag{70}$$

where l_0 is the length of the crack tip element, and A, B, D and E are the nodes on the crack tip element and at the opposite sides to where the displacements are computed (see Selvadurai & Mahyari, 1997).

6. Results

The analytical method developed in the previous sections was used to evaluate the quasistatic transient response of a poroelastic halfspace region during the injection of a fluid. The fluid is injected into either a planar circular region within a poroelastic halfspace domain, as discuss in section 3, or into a controlled, stable, axisymmetric, planar, circular fracture (see section 4). In order to present the numerical results for both problems, the following non-dimensional parameters are

Table 1
Material properties for the injection fluid and the rock*.

Material Properties	
Poisson's ratio	$\nu = 0.26$
Undrained Poisson's ratio	$\nu_u = 0.33$
Shear modulus	$G = 12.1 \times 10^9 \mathrm{N/m^2}$
Biot coefficient	$\alpha = 0.71$
Skempton's pore pressure parameter	$B = 0.46$
Hydraulic conductivity	$k = 8.12 \times 10^{-7}\ m/sec$
Unit weight of water	$\gamma_w = 9.8 \times 10^3\ N/m^3$
Bulk unit weight of the geomaterial	$\gamma_s = 22.1 \times 10^3 N/m^3$
Dynamic viscosity of the fluid	$\mu = 8.9 \times 10^{-4}\ N.sec/m^2$
Porosity	$n = 0.16$
Uniaxial compressive strength of the intact rock	$\sigma_{ci} = 37.9\,\mathrm{MPa}$
Storage coefficient	$S_s = 2.78 \times 10^{-9}\ \mathrm{m^2/N}$

* The quantities for Indiana limestone are a combination of measured and calculated values compiled by Hart and Wang (1995), and Głowacki and Selvadurai (2016).

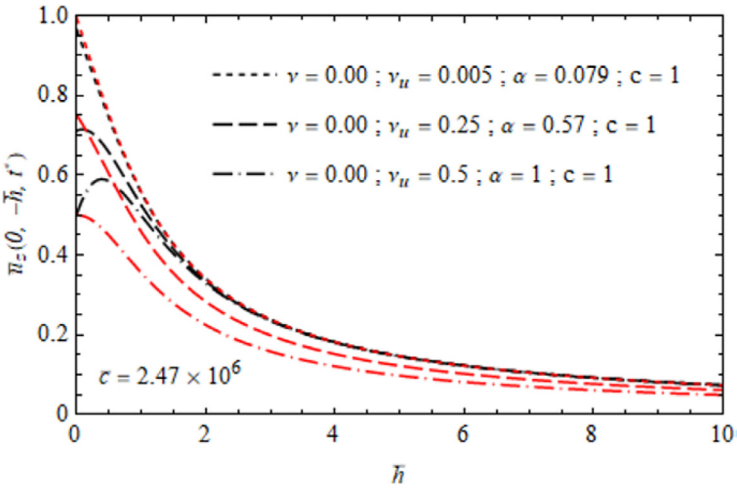

Fig. 6. Variation in the surface axial displacement vs. injection depth for different Poisson's ratios (red lines: $t^* = 10^{-2}$; black lines: $t^* = 10^4$). (For interpretation of the references to colour in this figure legend, the reader is referred to the web version of this article.)

introduced:

$$\begin{aligned}
&\bar{h} = h/a \quad ; \quad \bar{r} = r/a \quad ; \quad \bar{z} = z/a \quad ; \quad \bar{c} = c/ka \quad ; \quad t^* = ct/a^2 \\
&\bar{K}_{\mathrm{I}}(t^*) = a^{3/2} K_{\mathrm{I}}/p_0 \quad ; \quad \bar{K}_{II}(t^*) = \sqrt{2a} K_{\mathrm{I}}/\sqrt{\pi}\, p_0 \\
&p(\bar{r},\ \bar{z},\ t^*) = p(r,\ z,\ t)/p_0 \quad ; \quad \bar{u}_i(\bar{r},\ \bar{z},\ t^*) = G u_i(r,\ z,\ t)/a\, p_0 \quad ; \quad i = r,\ z \\
&\bar{\sigma}'_{ij}(\bar{r},\ \bar{z},\ t^*) = \sigma'_{ij}(r,\ z,\ t)/p_0 \quad ; \quad i,\ j = r,\ z
\end{aligned} \tag{71}$$

The fluid in the fracture and the interstitial pore space have similar rheological characteristics. In the results, the geological storage formation has properties similar to Indiana limestone as given in Table 1.

6.1. Fluid Injection within an internal circular region

Fig. 6 shows the variation in the maximum surface heave against the normalized injection depth for different values of Poisson's ratio. For all injection depths, with the exception of $\bar{h}$ smaller than 1, the long-term $t^* = 10^4$ surface displacement (black lines) is smaller than the short-term response at $t^* = 10^{-2}$ (red lines). When $\bar{h}$ is sufficiently small, the long-term surface heave reduces in value compared to deeper injections due to the pore pressure dissipation close to the surface of the halfspace region. For a fixed value of the drained Poisson's ratio, the results show larger surface displacements for smaller undrained Poisson's ratios, and the difference for short and long-term responses at $\bar{h} = 0$ are 47 % and 42.5 %, respectively. However, only a slight decrease of about 0.035 % and 5.1 % is observed in the short and long-term surface heave, respectively, when the drained Poisson's ratio increases from 0 to 0.495. The upper bound for the normalized surface heave is found for the case with $(\nu,\ \nu_u) = (0.00,\ 0.005)$.

Figs. 7 and 8 illustrate the short-term and long-term responses of the axial and radial surface displacements for different depths of injections (i.e. $\bar{h} = 1$ to 5). It can be seen from Fig. 7 that the surface heave is greatly influenced by a change in the depth of injection. Results show that the short-term and long-term maximum surface heave when the injection is made

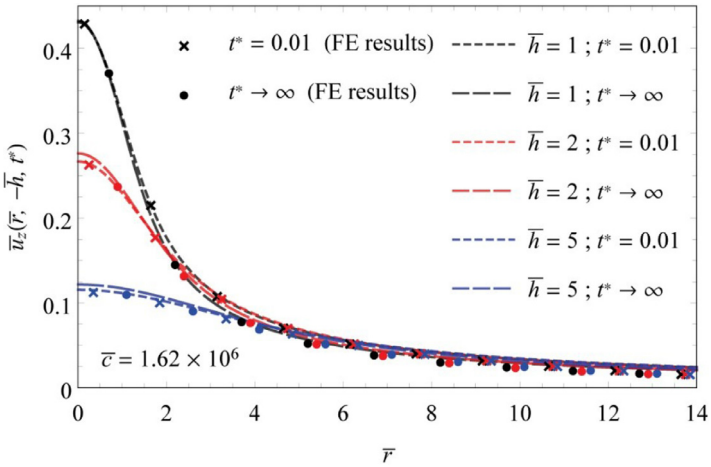

Fig. 7. Variation in the surface axial displacement due to fluid injection into a circular region (black markers: $\bar{h} = 1$ red markers: $\bar{h} = 2$ blue markers: $\bar{h} = 5$). (For interpretation of the references to colour in this figure legend, the reader is referred to the web version of this article.)

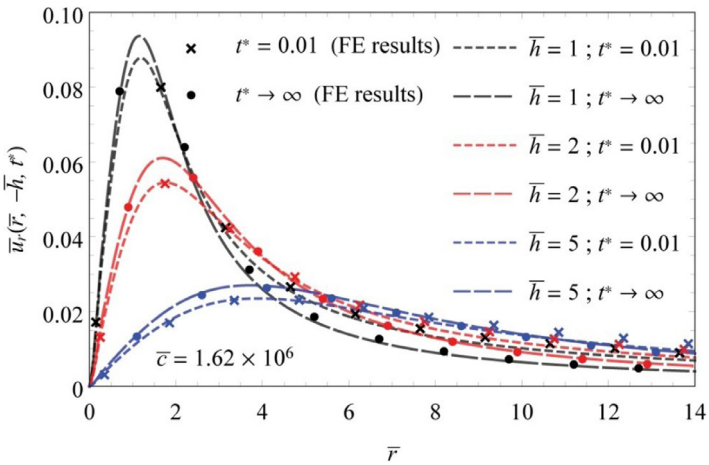

Fig. 8. Variation in the surface radial displacement due to fluid injection into a circular region (black markers: $\bar{h} = 1$ red markers: $\bar{h} = 2$ blue markers: $\bar{h} = 5$). (For interpretation of the references to colour in this figure legend, the reader is referred to the web version of this article.)

at $\bar{h} = 1$ are, respectively, 31.5 % and 31 % larger than the injection at $\bar{h} = 5$. [We note that in the limit as $\bar{h}$ reaches the value of 20, the injection will have a very negligible influence on surface displacements in the axial and radial directions.] The corresponding computational results are given for both short-term and long-term responses and show good agreement with the theoretical results.

Fig. 9 shows the variation of the surface axial displacement with time at different injection depths. The corresponding computational results are denoted by black markers and are in good agreement with the theoretical results for all time factors $t^* \geq 10^{-2}$ with a maximum discrepancy of approximately 0.69 % for $\bar{h} = 1$. Within the same range of time factors, the discrepancy of the computational results with respect to the theoretical values reduces as the value of $\bar{h}$ increases and becomes 0.12 % when $\bar{h} = 10$. The accuracy of the computational results, however, decreases significantly at the very early stages of injection $t^* < 10^{-2}$ as it approaches the limit of incompressibility of the poroelastic medium. To account for this computational constraint, a mixed formulation should be implemented in the solution scheme (see e.g. Lee et al., 2017; Selvadurai & Samea, 2020 and the references therein).

In Fig. 10, the variation of the pore fluid pressure along the z-axis due to a unit rise of pore pressure within a circular region located at $\bar{h} = 1$ is shown. The pore fluid pressure increases in magnitude over time. The values, however, approach zero when the position $\bar{z}$ is larger than 4. A negative fluid pressure develops in the vicinity of the surface of the halfspace soon after application of the step pressure. This can be attributed to the incompressible behaviour of the material close to the injection zone due to the combined counter action of the solid phase and the permeating fluid to the injection pressure. When this region is subjected to an instantaneous fluid pressure, it experiences small frame deformations. In other words, the material becomes locally inhomogeneous shortly after the injection, with stiffer regions close to the injection zone. As time evolves, the applied pressure will redistribute within the medium leading to an increase in the pore pressure in regions

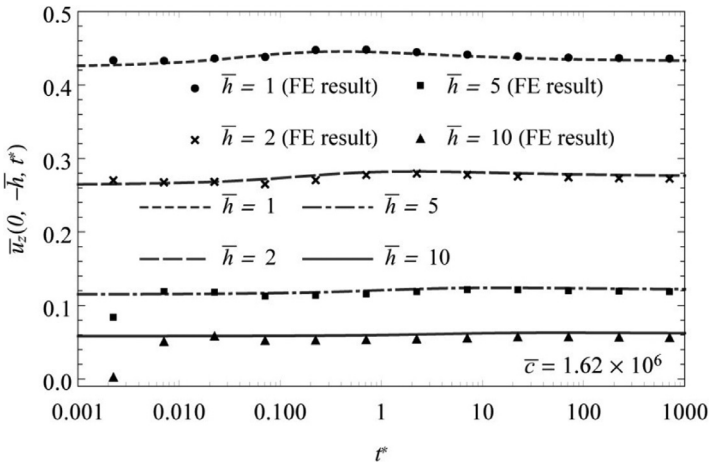

Fig. 9. Variation in the non-dimensional surface heave with time due to an injection into a circular region (markers denote the finite element modelling results).

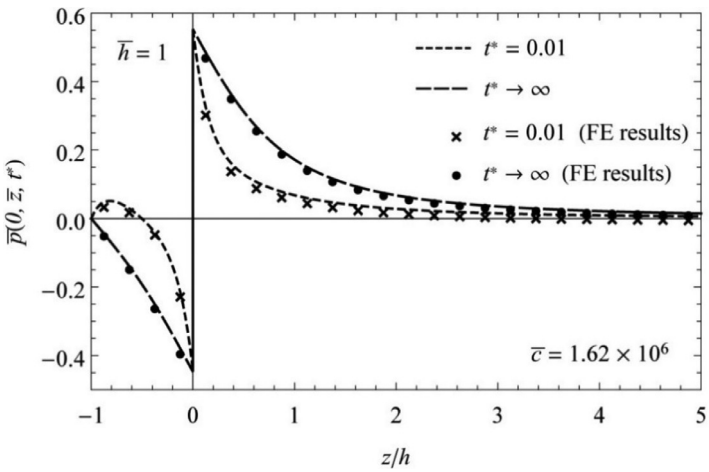

Fig. 10. Change in the pore fluid pressure with depth (markers denote the finite element modelling results).

close to the surface of the halfspace. The corresponding computational results for both short-term and long-term responses are also shown in Fig. 10 and are in reasonable agreement with the theoretical results.

The increase in the pore fluid pressure around the injection region results in a sudden decrease in the effective stresses at the injection plane. Figs.11 and 12 show that the axial effective stress at the injection region reduces but remains positive. The short-term and long-term radial effective stresses at the injection plane have negative values due to the fluid injection. As time progresses, a larger negative radial effective stress will be generated below the injection elevation at approximately $\bar{z} = 0.8$. Both the axial and radial effective stresses approach very small values when $\bar{z}$ is larger than 5. The computational results are in very good agreement with the theoretical ones; however, this congruence is particularly noticeable for longer times.

The susceptibility to crack initiation within the injection zone can be examined by using an appropriate failure criterion expressed in terms of principal effective stresses. The choice of a specific failure criterion will ultimately depend on the particular rock or geomaterial that is being investigated. Various failure criteria have been proposed over the past century to describe the initiation of failure and the development of plastic flow in geomaterials and dilatant interfaces (see e.g. Chen & Baladi, 1985; Darve, 1990; Desai & Siriwardane, 1984; Drucker & Prager, 1952; Pande et al., 1990; Schofield & Wroth, 1968) Recent advances in this area are given by Davis and Selvadurai (2005), Pietruszczak (2010), Selvadurai (2020, 2021) and Selvadurai et al. (2018). In the case of brittle rocks that are dominated by brittle fracture phenomena, the previously cited articles, articles by Brace (1960), Brace and Bombalakis (1963) and the volumes by Jaeger (1972) and Jaeger et al. (2007) can be consulted. A failure criterion that is extensively used in the rock mechanics literature is the Hoek-Brown criterion (Hoek & Brown, 2019). The stresses contributing to failure generation in the poroelastic medium are identified as the stresses acting in the skeleton. In this study, the effective stress is used in the calculations of the failure criterion. The

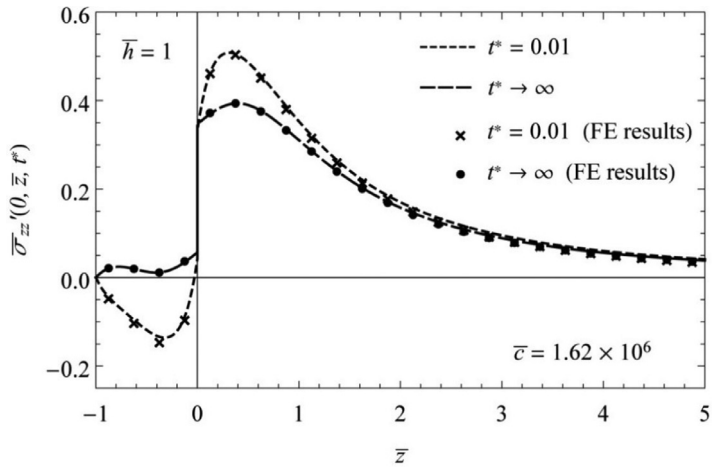

Fig. 11. Change in the normal effective stress with depth (markers denote the finite element modelling results).

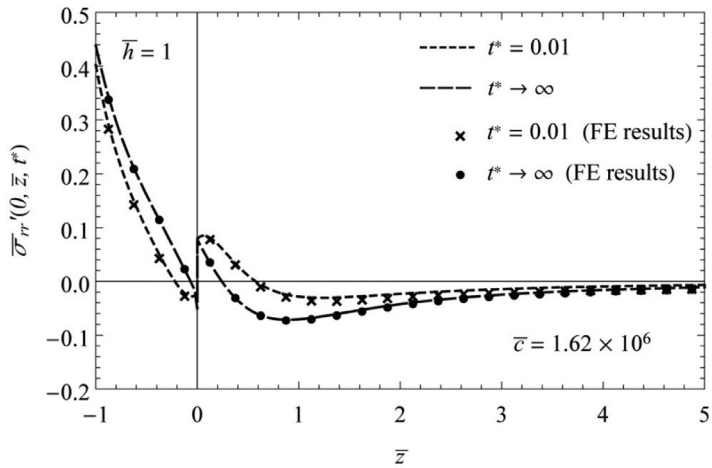

Fig. 12. Change in the radial effective stress with depth (markers denote the finite element modelling results).

failure envelope can be written as

$$\sigma'_{1f} = \sigma'_{3f} + \sigma_{ci}\left(m\frac{\sigma'_{3f}}{\sigma_{ci}} + 1\right)^{0.5}. \tag{72}$$

In this equation, σ'_{1f} and σ'_{3f}, are, respectively, the major and minor principal effective stresses at failure; m can be defined as a negative exponent function proposed by Peng et al., (2014) which, in the case of Indiana limestone, is equal to $7.8\,e^{-\sigma'_{3f}/22.5}$. The Hoek-Brown criterion can be represented in the form of the k_f-line in terms of $p' = (\sigma'_1 + \sigma'_3)/2$ and $q' = (\sigma'_1 - \sigma'_3)/2$. The k_f-line corresponds to the stress state that will promote the nucleation of a fracture. As is evident, the injection pressure and the ability of pore fluid pressure dissipation, which is controlled by the permeability of the poroelastic medium, will promote fracture nucleation according to a relatively elementary criterion.

Fig. 13 shows the Hoek-Brown criterion for the point located at the center of a circular region ($\bar{r} = 0$; $a = 10\,\text{m}$) when the injection is made within an Indiana limestone formation at $\bar{h} = 1$. The stress path is a function of time and is represented in the form of a line with its slope being

$$\frac{dq'}{dp'} = \frac{d\sigma'_1 - d\sigma'_3}{d\sigma'_1 + d\sigma'_3}. \tag{73}$$

The stress path approaches the k_f-line as the pressure increases and failure takes place at the center of the injection region when the two lines intersect. The maximum pressure and its corresponding axial flow rate at failure (Q_f) are, respectively, equal to 131.2 kPa and 0.667 m^3/hr as $t \to \infty$. The injection pressure necessary to nucleate a fracture at the center of the pressurized region is higher at the limit as $t \to 0$. The maximum injection pressure, however, decreases with time as

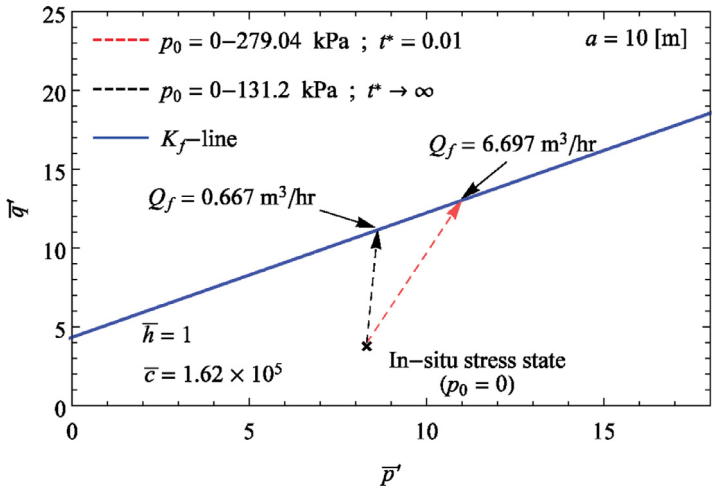

Fig. 13. The Hoek-Brown criterion and the stress path.

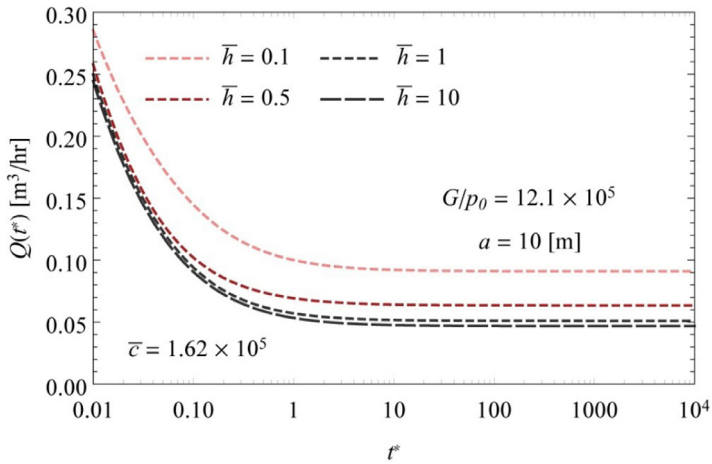

Fig. 14. Variation of flow rate with time at different injection depths for $p_0 = 10$ kPa.

$t \to \infty$. Hence, the maximum pressure or its corresponding flow rate at the injection site should be limited to the failure pressure and flow rate at $t \to \infty$.

The variation in the axial flow rate at the injection region with time is given in Fig. 14. When the fluid is injected within the injection site, the leak-off volume reduces until $t^* = 1$ and then stabilizes over the entire time range. It is observed that the leak-off volume is larger for shallower injection depths due to the proximity of the injection region to the surface of the halfspace.

6.2. Fluid Injection into a penny-shaped crack

Figs. 15–18 show the non-dimensional transient Mode I and Mode II stress intensity factors for both loading cases versus time and for different Poisson's ratios. The injection is assumed to be made into a penny-shaped crack within a poroelastic halfspace region at $\bar{h} = 1$. Results yield higher stress intensity factors for larger undrained Poisson's ratios and a fixed value for the drained Poisson's ratio. Moreover, both Mode I and Mode II stress intensity factors (SIFs) reach a constant value as $t^* \to \infty$. When $(\nu, \nu_u) = (0.0, 0.005)$, the stress intensity factors show slight changes with time for both Mode I and Mode II SIFs.

Figs. 19–22 illustrate the transient change in the Mode I and Mode II stress intensity factors for both loading cases and for different injection depths, $\bar{h}$. The results show a decease in both Mode I and Mode II stress intensity factors as $\bar{h}$ increases. Also, as $\bar{h}$ increases and tends to infinity, the results for the problem of fluid injection into a poroelastic full space region will be attained. The Mode II stress intensity factor is zero for relatively deep injections where $\bar{h} \geq 5$. The corresponding computational results for both stress intensity factors are also illustrated and slightly overestimate the theoretical results. However, the maximum deviation of the computational results with respect to the theoretical results is around 2.5 %.

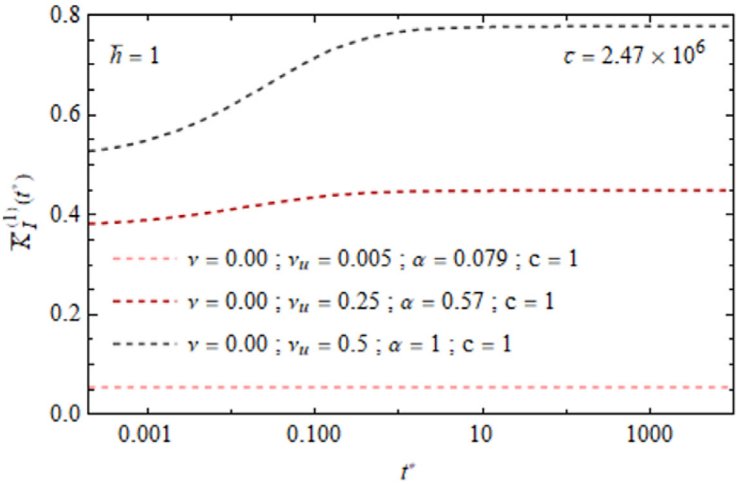

Fig. 15. Variation in the Mode I stress intensity factor for loading Case 1 against time for different Poisson's ratios.

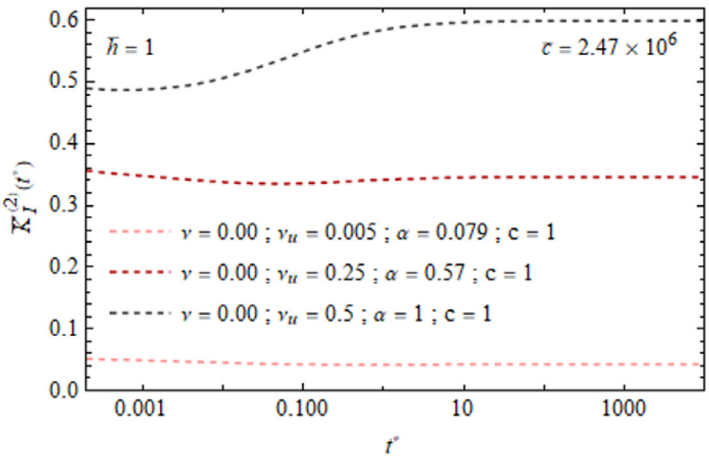

Fig. 16. Variation in the Mode I stress intensity factor for loading Case 2 against time for different Poisson's ratios.

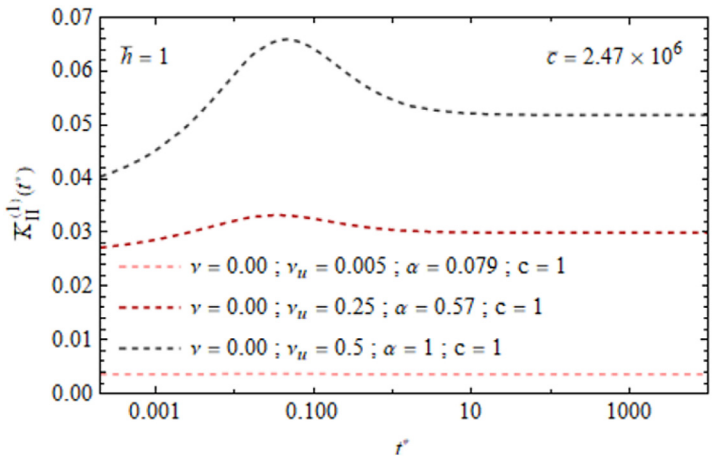

Fig. 17. Variation in the Mode II stress intensity factor for loading Case 1 against time for different Poisson's ratios.

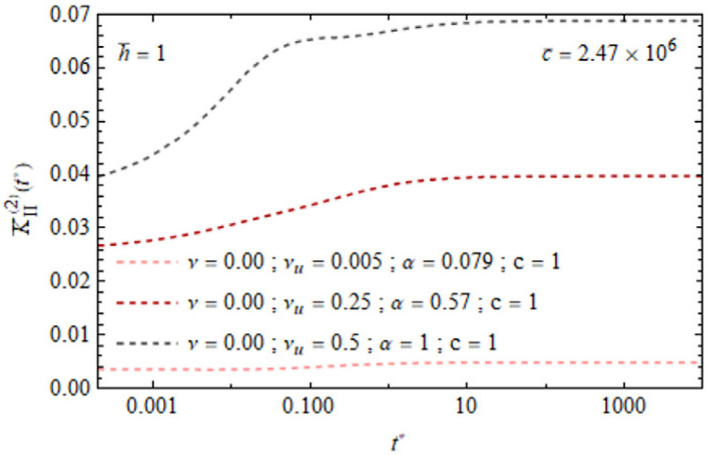

Fig. 18. Variation in the Mode II stress intensity factor for loading Case 2 against time for different Poisson's ratios.

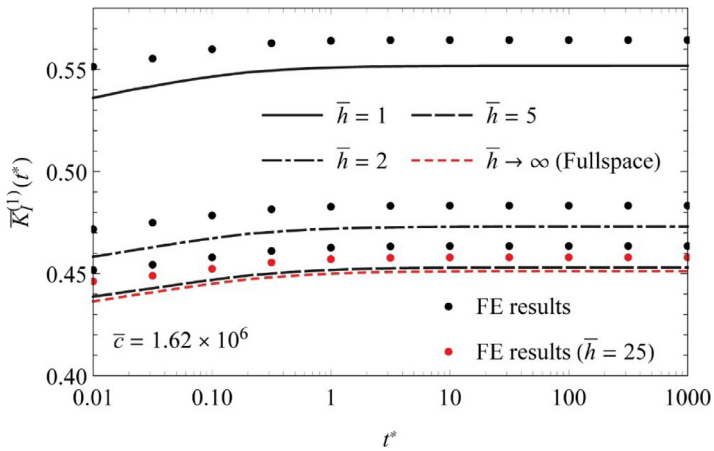

Fig. 19. Variation in the Mode I stress intensity factor for loading Case 1 with time for different injection depths (markers denote the finite element modelling results).

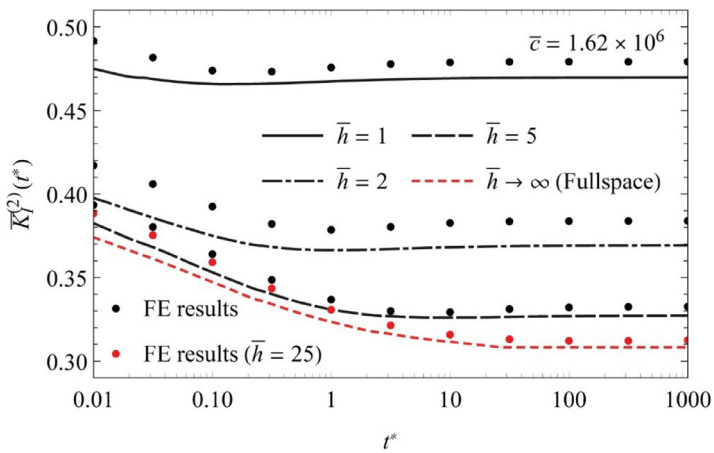

Fig. 20. Variation in the Mode I stress intensity factor for loading Case 2 with time for different injection depths (markers denote the finite element modelling results).

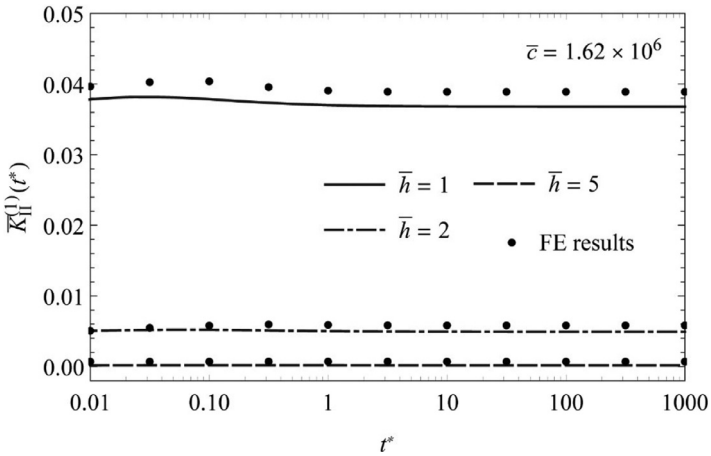

Fig. 21. Variation in the Mode II stress intensity factor for loading Case 1 with time for different injection depths (markers denote the finite element modelling results).

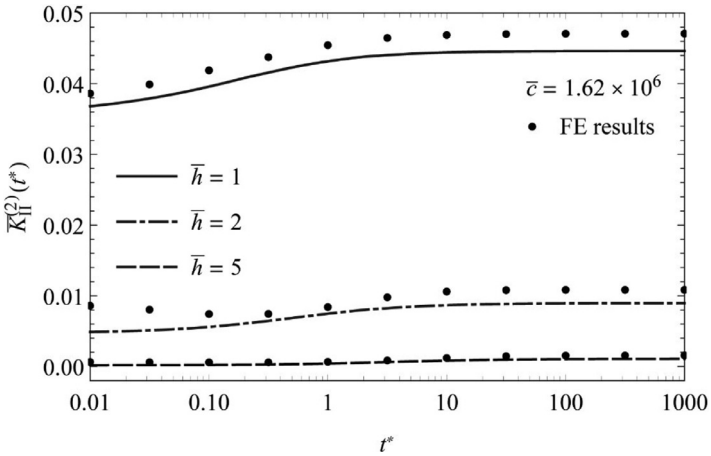

Fig. 22. Variation in the Mode II stress intensity factor for loading Case 2 with time for different injection depths (markers denote the finite element modelling results).

Figs. 23–26 illustrate the axial and radial surface displacement responses for both loading cases and at two different injection depths (i.e. $\bar{h} = 1$ and 2). As expected, Figs. 23 and 24 show that the amplitude of the free surface uplift is considerably influenced by a change in $\bar{h}$. Results show that the maximum value for the long-term surface axial displacement for Case 1 loading when the injection is made at $\bar{h} = 1$ is more than two times (around 215 %) larger than when the injection is made at $\bar{h} = 2$. For Case 2, however, the maximum long-term surface axial displacement for $\bar{h} = 1$ is about 80 % larger than for $\bar{h} = 2$. Also, in the limit as $\bar{r}$ reaches a value of around 5, the injection will have a negligible influence on the surface displacements in the axial and radial directions for loading Case 1. The corresponding computational results are denoted by black markers and they show good quantitative agreement with the theoretical results for all time factors $t^* \geq 10^{-2}$. The accuracy of the computational results reduces appreciably as the limit of incompressibility of the poroelastic medium is approached (i.e. as $t^* \to 0$). A comparison between Figs. 7, 23, and 24 shows that the maximum surface heave due to injection into a penny-shaped crack located at $\bar{h} = 1$ is around 2.68 % larger for Case 1 loading, and 43.99 % larger for Case 2 loading compared to the surface heave due to injection into a circular plane. This is, however, not the case for $\bar{h} = 2$, which for Case 1 loading, decreases by 95.70 % but increases by 20.18 % for Case 2.

The fracture opening profile as a function of time t^* and injection depth $\bar{h}$ are plotted in Figs. 27 and 28 for loading Cases 1 and 2, respectively. Both short-term and long-term opening profiles are plotted. Fig. 28 shows that for $\bar{h} = 1$, the normalized crack surface axial displacement defined by $\bar{\Delta}_c[= \bar{u}_z^{(i)}(r, 0, t) - \bar{u}_z^{(i)}(a, 0, t)]; \quad i = \mathrm{L}, \mathrm{H}; \quad r < a$ is essentially concentrated on the upper face of the crack. We observe that as $\bar{h}$ increases, the results for the fracture opening profile at both the short-term and long-term limits approaches a symmetric ellipse. In fact, a deviation from a symmetric ellipse with a decrease in $\bar{h}$ reflects the decreases in the resistance of the rock layer to crack opening for a given pressure.

The solution of the pressurized fracture problem can also be treated by decomposing the boundary conditions at the crack region into two separate fundamental loading scenarios. The complete solution of the problem can be obtained by

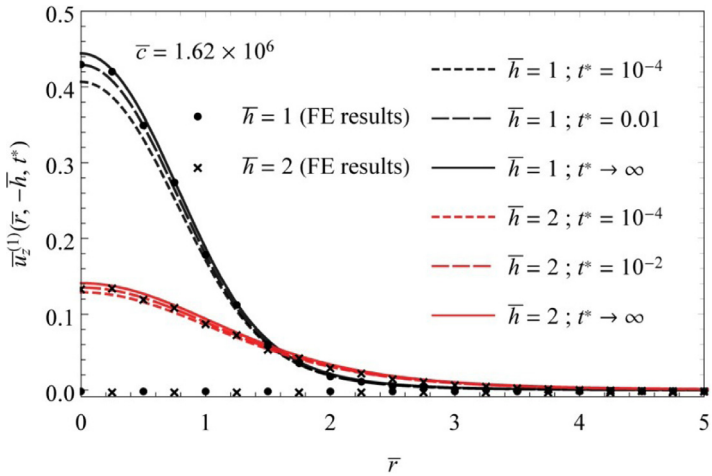

Fig. 23. Surface heave due to injection into a penny-shaped crack within a poroelastic halfspace region for loading Case 1 (markers denote the finite element modelling results).

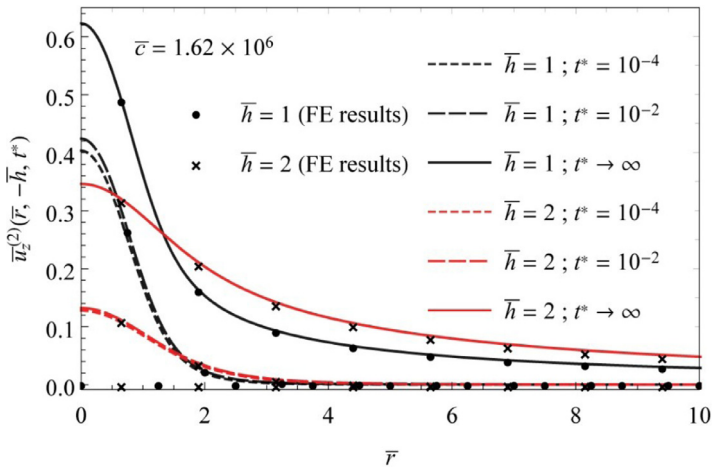

Fig. 24. Surface heave due to injection into a penny-shaped crack within a poroelastic halfspace region for loading Case 2 (markers denote the finite element modelling results).

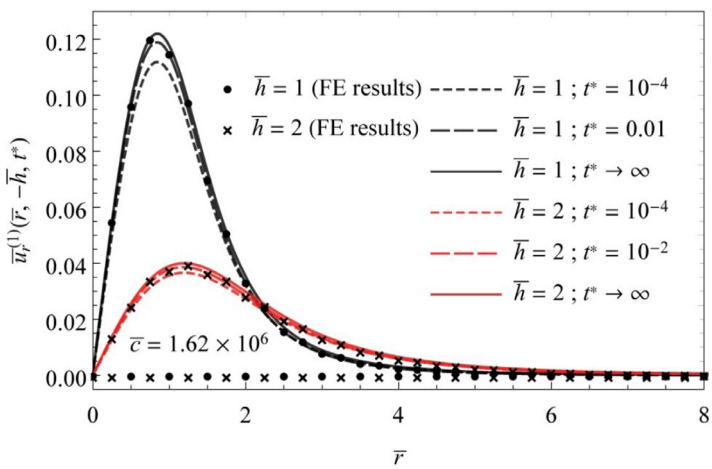

Fig. 25. Change in surface radial displacement due to injection into a penny-shaped crack within a poroelastic halfspace region for loading Case 1 (markers denote the finite element modelling results).

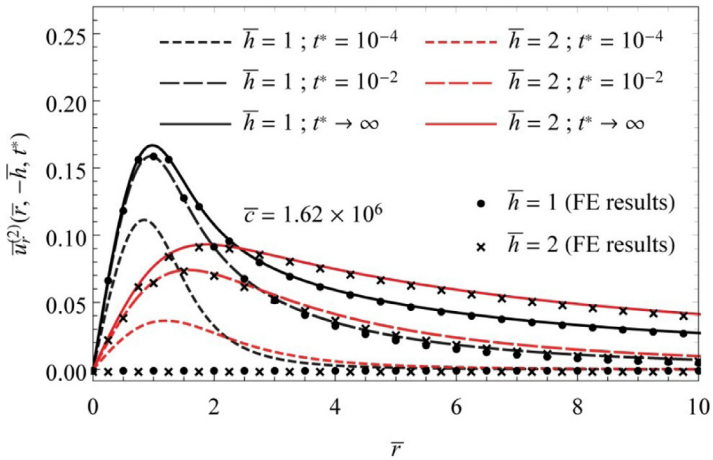

Fig. 26. Change in surface radial displacement due to injection into a penny-shaped crack within a poroelastic halfspace region for loading Case 2 (markers denote the finite element modelling results).

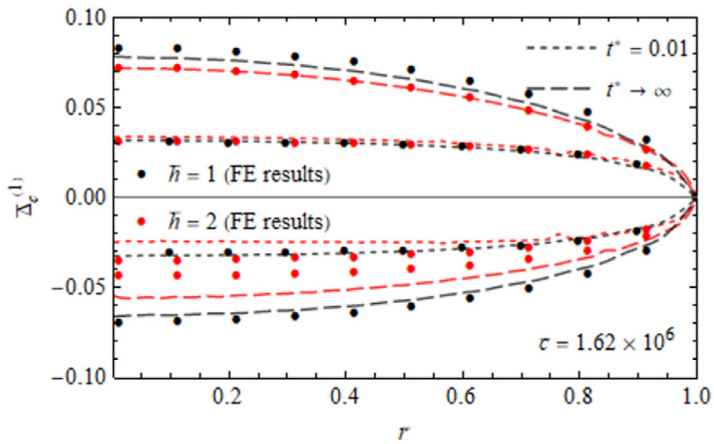

Fig. 27. Change in normalized fracture profile for loading Case 1 (scenario A) at different time factors t^* (black lines: $\bar{h} = 1$ Red lines: $\bar{h} = 2$). (For interpretation of the references to colour in this figure legend, the reader is referred to the web version of this article.)

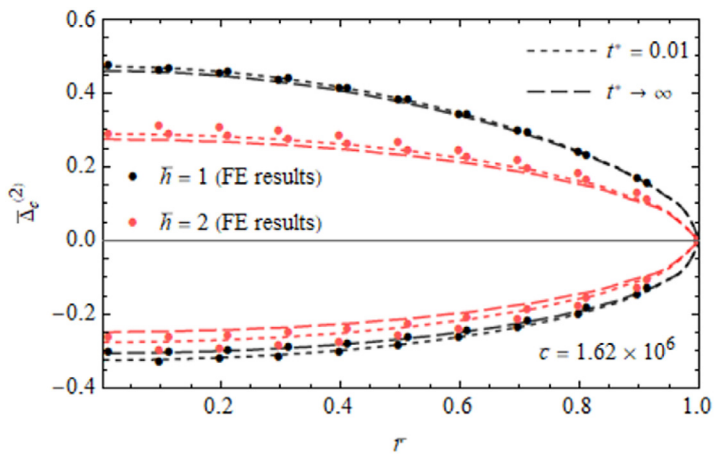

Fig. 28. Change in normalized fracture profile for loading Case 2 at different time factors t^* (black lines: $\bar{h} = 1$ Red lines: $\bar{h} = 2$). (For interpretation of the references to colour in this figure legend, the reader is referred to the web version of this article.)

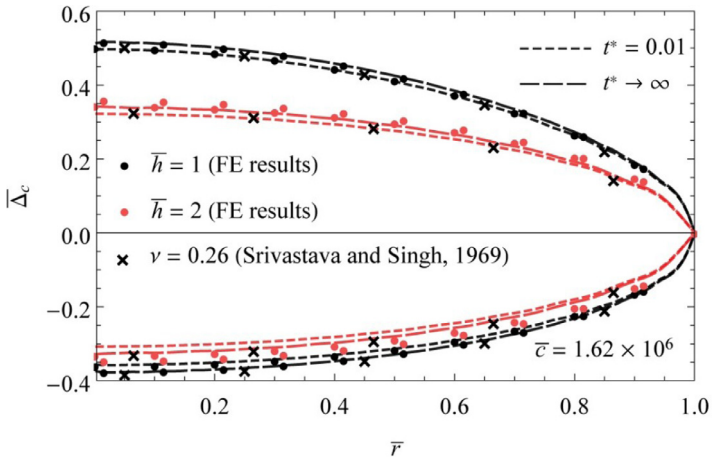

Fig. 29. Change in normalized fracture profile for scenario B (black lines: $\bar{h} = 1$ Red lines: $\bar{h} = 2$). (For interpretation of the references to colour in this figure legend, the reader is referred to the web version of this article.)

superposing the results of these two scenarios. The presence of the injection fluid within the crack region has two loading effects; it not only represents the pore fluid pressure at the crack boundary, but also represents the axial stress acting on the same boundary. The first scenario (A) thus corresponds to the application of a pore pressure on the crack faces as discussed in Case 1, i.e. $p^{(L)}(r,0,t) = p^{(H)}(r,0,t) = p_0\,\mathrm{H}(t)$ and $\sigma_{zz}^{(L)}(r,0,t) = \sigma_{zz}^{(H)}(r,0,t) = 0$; and the second scenario (B) corresponds to the application of a normal stress on the crack boundary $\sigma_{zz}^{(L)}(r,0,t) = \sigma_{zz}^{(H)}(r,0,t) = \sigma\,\mathrm{H}(t) = \alpha\,p_0\mathrm{H}(t)$ and $p^{(L)}(r,0,t) = p^{(H)}(r,0,t) = 0$. The subtraction of the results for these two scenarios corresponds to the Case 2 discussed in Section 4. Scenario A represents a leak-off process and causes a dilation of the porous material as a result of it being constrained from expansion, and hence the medium around the injection region experiences an increase in the confining compressive stress and, consequently, a higher fracture pressure. This excess pressure at the crack boundary, otherwise known as the *back-stress* effect, was first discussed by Cleary (1979) and later extended by Detournay et al. (1989) to investigate the borehole problem in a poroelastic medium and by Detournay and Cheng (1991) to examine the Griffith crack problem. The back-stress effect results in a decrease in the crack volume (crack boundary displacement) at early stages of injection followed by a progressive time-dependent evolution of the crack geometry as a result of pressure redistribution in regions farther away from the injection zone, as shown in Fig. 27. The early stage decrease in the crack volume increases the pore fluid pressure at the injection region. This effect is analogous to the Mandel-Cryer effect that is observed in poroelastic, thermo-poroelastic, poroelasto-plastic and poro-hyperelastic materials (Mandel, 1953; Cryer, 1963; Abousleiman et al., 1996; De Josselin de Jong, 1953, 1957; Gibson et al., 1963; Holzbecher, 2016; Najari & Selvadurai, 2014; Selvadurai & Najari, 2017; Selvadurai & Nguyen, 1995; Selvadurai & Shirazi, 2004; Selvadurai & Suvorov, 2012, 2014, 2016b; Verruijt, 2015; Yue et al., 1994), where a time-dependent transfer of the pore fluid pressure to the porous skeleton leads to a compression of the skeleton and an attendant increase in the pore fluid pressure within a contained fluid region.

Fig. 29 illustrates the normalized transient fracture profile for a penny-shaped crack within a poroelastic halfspace region subjected to a purely mechanical loading $\alpha\,p_0\mathrm{H}(t)$ (scenario B). As $t^* \to \infty$, the solution for the poroelasticity problem recovers the solution for a penny-shaped crack within an elastic halfspace region subjected to a mechanical load equal to $\alpha\,p_0$ given by Srivastava and Singh (1969). The elasticity solution is shown by cross markers.

The Figs. 30 and 31 show the variation of the pore fluid pressure along the z-axis due to fluid injection into the poroelastic halfspace region for different values of the non-dimensional time factor t^*. Soon after application of the pressure p_0 within the crack, a small region close to the surface will experience a negative pore fluid pressure distribution. With increasing time, the pore fluid pressure becomes positive everywhere within the halfspace, with its maximum always at the injection level. The values, however, decay as $\bar{z}$ increases in the far field. The corresponding computational results are shown as cross markers and as discussed earlier, the accuracy of the finite element results drops significantly as $t^* \to 0$. This is more pronounced for loading Case 2 than Case 1 (scenario A). As shown in Fig. 30, the Case 1 pore fluid pressure at the injection region grows by 3.65 % immediately after the injection (at $t^* = 10^{-4}$) and reduces with time. The pore fluid pressure remains equal to $\bar{p}^{(1)}(0,\ \bar{z},\ t^*) = 1$ for $t^* \geq 10^{-2}$.

The increase in the pore fluid pressure around the injection region results in a decrease in the effective stresses. Figs. 32–35 show the change in the axial and radial effective stress along the z-axis due to fluid injection. The results show that the effective stresses reduce to negative values. The back-stress effect results in a 2.6 % reduction in the axial effective stresses at the early stages of the injection at $t^* = 10^{-4}$. The reduction in the radial effective stress is more pronounced and is equal to and 27.1 % at $t^* = 10^{-4}$ and is equal to 9 % at $t^* = 10^{-2}$.

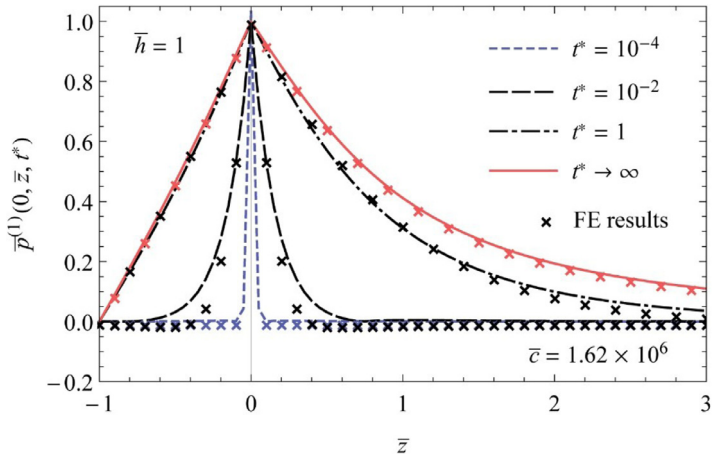

Fig. 30. Change in the pore fluid pressure with $\bar{z}$ (Loading Case 1 (scenario A) - markers denote the finite element modelling results).

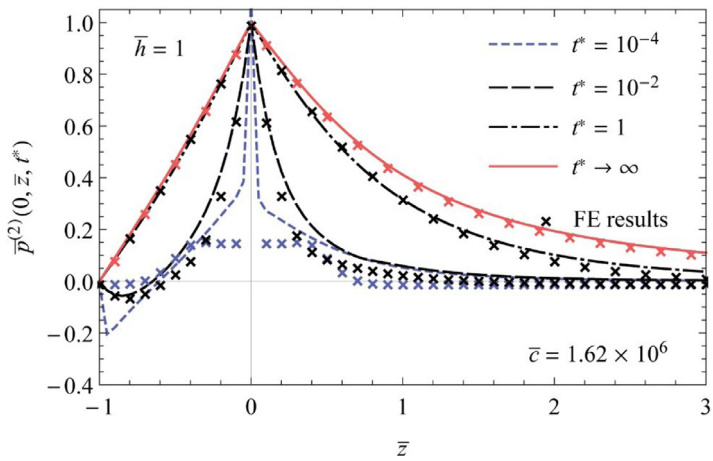

Fig. 31. Change in the pore fluid pressure with $\bar{z}$ (Loading Case 2 - markers denote the finite element modelling results).

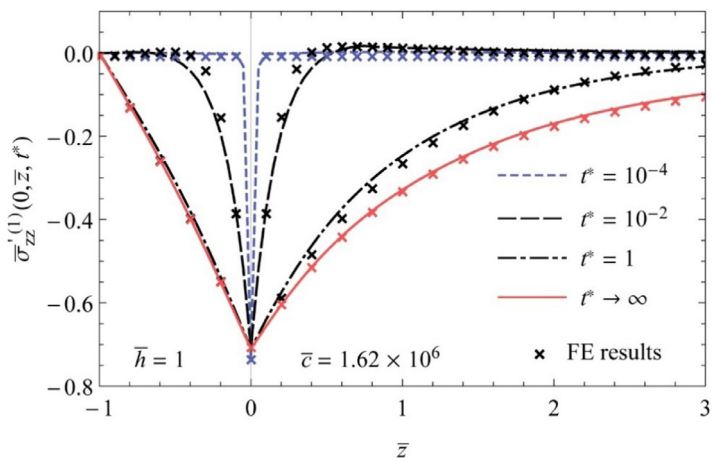

Fig. 32. Change in the axial effective stresses with $\bar{z}$ (Loading Case 1 (scenario A) - markers denote the finite element modelling results).

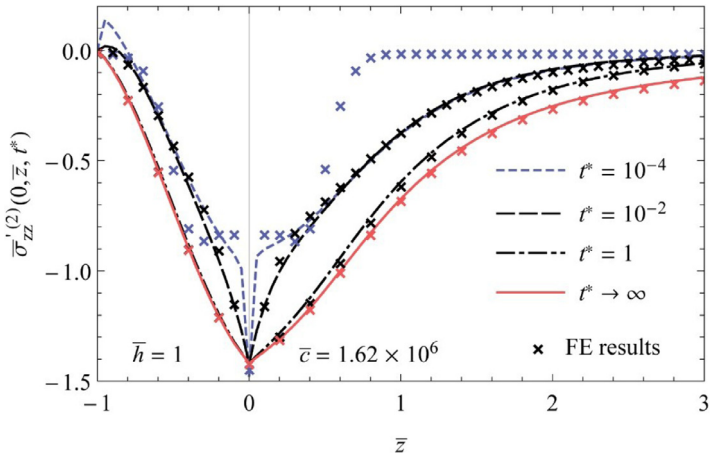

Fig. 33. Change in the axial effective stresses with $\bar{z}$ (Loading Case 2 - markers denote the finite element modelling results).

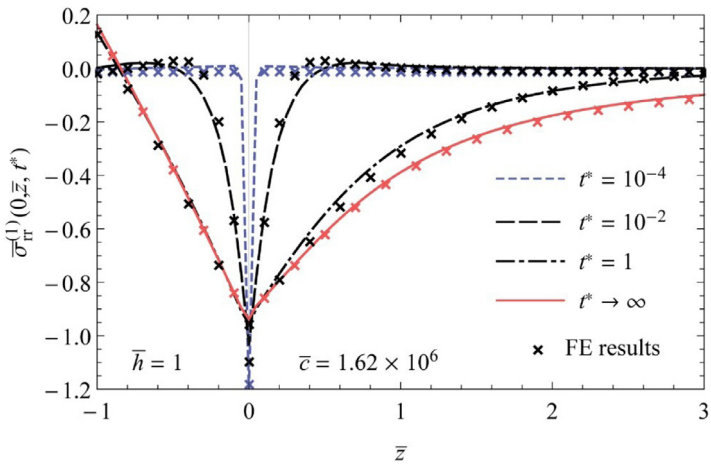

Fig. 34. Change in the radial effective stresses with $\bar{z}$ (Loading Case 1 (scenario A) - markers denote the finite element modelling results).

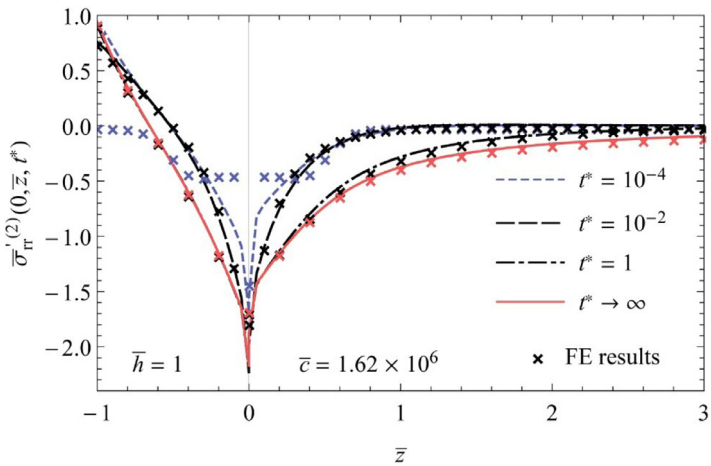

Fig. 35. Change in the radial effective stresses with $\bar{z}$ (Loading Case 2 - markers denote the finite element modelling results).

7. Conclusions

Fluid injection into a saturated poroelastic medium has a wide range of engineering applications including activities related to extraction of oil and gas reserves, and deep injection of wastewater, fluidized greenhouse gases and hazardous fluids into intact geologic formations. The engineering issues associated with these geosciences and geoengineering activities involve the application of pressures to the fluid-saturated poroelastic geologic formation. The paper, first deals with the problem of fluid injection within a poroelastic medium that would create the skeletal stress state necessary to initiate fracture. Attention is focused on the influence of the pore fluid pressure, the drained and undrained Poisson's ratios, and the depth of injection on the surface displacements. The change in the skeletal stresses surrounding the injection region and the leak-off volume from the injection region are obtained and the propensity of fracture nucleation at the injection plane is investigated by applying an appropriate failure criterion. The theoretical solutions are also compared with the results obtained from a conventional finite-element software package. The computational results show good quantitative agreement with the theoretical results for all time factors $t^* \geq 10^{-2}$. The paper then proceeds with the mathematical development of the mechanics of cracks in a poroelastic halfspace region. The pore fluid pressure and traction boundary conditions associated with the surfaces of the crack and the surface of the halfspace are correctly applied. Two loading scenarios were considered for the choice of the traction boundary conditions at the surface of the crack: (i) when both the porous skeleton and the pore fluid take part in the transfer of the applied pressure within the injection region; and (ii) when the boundary condition assumes that the effective stress is zero at the injection region and the applied pressure is transferred only through the interstitial fluid. For both loading scenarios, it is shown that the adoption of finite transforms in a Hankel and Laplace transform space leads to the development of a system of coupled Fredholm integral Eqs.. The development of a completely analytical solution of this system is an unrealistic expectation. The coupled system is numerically solved to generate results of interest to engineering applications. The numerical solution of the system of integral Eqs. is non-routine and requires access to supercomputing facilities. The Laplace transform inversion procedure was used in previous studies and the approaches were successfully implemented to study poroelastic contact problems. The numerical results were generated to demonstrate the time-dependent evolution of stress intensity factors at the tip of the penny-shaped crack, the time-dependent surface deformations of the halfspace resulting from internal pressurization and the deformed profile of the crack. Although numerical techniques are ultimately needed to solve the system of coupled integral Eqs. and for the Laplace transform inversion, they can be regarded as bona-fide analytical results for this class of poroelastic mixed boundary value problems, thus providing a suitable set of results that can be classified as being of a benchmark quality. With this in mind, the same problems were solved using a widely adopted computational multi-physics finite element code. The results for the time-dependent evolution of the stress intensity factors, surface deformations and crack deformations all conform closely to the results derived from the analytical approach, except for the short-term responses of the medium as $t^* \to 0$. This computational constraint can be eradicated by employing a mixed formulation in the solution scheme. The limiting results for the poroelasticity problem as $t^* \to 0$ and $t^* \to \infty$ also agree with the analogous elasticity solutions developed separately and by other researchers. The processes that are inherent in both problems are complicated and any analytical development can proceed only by examining mathematical problems under highly specialized configurations.

Data accessibility

The computer codes and subroutines can be accessed at the following sites: https://www.mcgill.ca/civil/selvadurai/research-repository.

Author's contribution

Problems discussed in this paper were conceived by APSS. The formulation of the problems and the development of the governing Eqs. and the reduction to the sets of Fredholm integral Eqs. were provided by PS. Numerical solution of the integral Eqs. and computational modeling were carried out by PS. The paper was written by APSS and PS. Both authors read and approved the final manuscript.

Declaration of Competing Interest

We have no relevant interest(s) to disclose.

Acknowledgments

The research reported in this paper was supported by the NSERC Discovery Grant and the Distinguished James McGill Research Chairs support Awarded to APS Selvadurai. The McGill Engineering Doctoral Award granted to P Samea is also acknowledged. The computations associated with the research were performed through access to the computing support provided by Calcul Québec and Compute Canada HPC facilities and this support is gratefully acknowledged.

Funding

The work described in this paper was supported by an NSERC *Discovery Grant* and the Distinguished James McGill Research Chairs support awarded to the first author. The second author acknowledges the research support provided by a *McGill Engineering Doctoral Award*.

Appendix A

The integral representations, for the axial displacements, the stress components and the pore pressure can be written as:

$$u_z^{(m)}(r,z,t) = \int_{\chi+i\infty}^{\chi-i\infty}\int_0^\infty \xi\left\{-\frac{d}{dz}\tilde{\tilde{E}}^{(m)}(\xi,z,s) + \left(z\frac{d}{dz}-1\right)\tilde{\tilde{S}}^{(m)}(\xi,z,s)\right\}J_0(\xi r)e^{st}d\xi ds \quad ; \quad m = \mathrm{L},\ \mathrm{H} \tag{A.1}$$

$$u_r^{(m)}(r,z,t) = \int_{\chi-i\infty}^{\chi+i\infty}\int_0^\infty \xi^2\left\{\tilde{\tilde{E}}^{(m)}(\xi,z,s) - z\tilde{\tilde{S}}^{(m)}(\xi,z,s)\right\}J_1(\xi r)e^{st}d\xi\, ds \quad ; \ m = \mathrm{L},\ \mathrm{H} \tag{A.2}$$

$$\sigma_{zz}^{(m)}(r,z,t) = 2G\int_{\chi-i\infty}^{\chi+i\infty}\int_0^\infty \xi\left\{\xi^2\tilde{\tilde{E}}^{(m)}(\xi,z,s) - \left(z\frac{d^2}{dz^2}-\frac{d}{dz}\right)\tilde{\tilde{S}}^{(m)}(\xi,z,s)\right\}J_0(\xi r)e^{st}d\xi\, ds \quad ; \ m = \mathrm{L},\ \mathrm{H} \tag{A.3}$$

$$\sigma_{rz}^{(m)}(r,z,t) = 2G\int_{\chi-i\infty}^{\chi+i\infty}\int_0^\infty \xi^2\left\{-\frac{d}{dz}\tilde{\tilde{E}}^{(m)}(\xi,z,s) + z\frac{d}{dz}\tilde{\tilde{S}}^{(m)}(\xi,z,s)\right\}J_1(\xi r)e^{st}d\xi\, ds \quad ; \ m = \mathrm{L},\ \mathrm{H} \tag{A.4}$$

$$\begin{aligned}\sigma_{rr}^{(m)}(r,z,t) = {} & 2G\int_{\chi-i\infty}^{\chi+i\infty}\int_0^\infty \xi\left\{\left(\frac{\xi^2}{2}-\frac{d^2}{dz^2}\right)\tilde{\tilde{E}}^{(m)}(\xi,z,s) + \left(z\xi^2+\frac{d}{dz}\right)\tilde{\tilde{S}}^{(m)}(\xi,z,s)\right\}J_0(\xi r)e^{st}d\xi\, ds \\ & + G\int_{\chi-i\infty}^{\chi+i\infty}\int_0^\infty \xi\left\{\xi^2\tilde{\tilde{E}}^{(m)}(\xi,z,s) - z\xi^2\tilde{\tilde{S}}^{(m)}(\xi,z,s)\right\}J_2(\xi r)e^{st}d\xi\, ds \quad ; \ m = \mathrm{L},\ \mathrm{H}\end{aligned} \tag{A.5}$$

$$\begin{aligned}\sigma_{\theta\theta}^{(m)}(r,z,t) = {} & 2G\int_{\chi-i\infty}^{\chi+i\infty}\int_0^\infty \xi\left\{\left(\xi^2-\frac{d^2}{dz^2}\right)\tilde{\tilde{E}}^{(m)}(\xi,z,s) + \frac{d}{dz}\tilde{\tilde{S}}^{(m)}(\xi,z,s)\right\}J_0(\xi r)e^{st}d\xi\, ds \\ & - \frac{2G}{r}\int_{\chi-i\infty}^{\chi+i\infty}\int_0^\infty \xi^2\left\{\tilde{\tilde{E}}^{(m)}(\xi,z,s) - z\tilde{\tilde{S}}^{(m)}(\xi,z,s)\right\}J_1(\xi r)e^{st}d\xi\, ds \quad ; \ m = \mathrm{L},\ \mathrm{H}\end{aligned} \tag{A.6}$$

$$p^{(m)}(r,z,t) = \frac{2G}{\alpha}\int_{\chi-i\infty}^{\chi+i\infty}\int_0^\infty \xi\left\{\frac{d}{dz}\tilde{\tilde{S}}^{(m)}(\xi,z,s) - \eta\left(-\xi^2+\frac{d^2}{dz^2}\right)\tilde{\tilde{E}}^{(m)}(\xi,z,s)\right\}J_0(\xi r)e^{st}d\xi\, ds \quad ; \ m = \mathrm{L},\ \mathrm{H} \tag{A.7}$$

in which χ is a real number associated with the Bromwich integral. The expressions for $\tilde{\tilde{E}}^{(m)}(\xi,z,s)$ and $\tilde{\tilde{S}}^{(m)}(\xi,z,s)$ are given in (37)-(40) and the constants $A_1^{(\mathrm{L})}$, $B_1^{(L)}$, ..., $A_3^{(\mathrm{H})}$ can be found in the website.

Appendix B

With the aid of the representations (54)-(56) and the requirements

$$\lim_{\rho\to 0}\left\{\tilde{\phi}_1(\rho,s),\ \tilde{\phi}_2(\rho,s)\right\} = 0 \qquad ; \qquad \lim_{\rho\to 0}\left[\rho^{1/2}\tilde{\phi}_3(\rho,s)\right] = 0, \tag{B.1}$$

the system of dual integral Eqs. (48)-(53) can be reduced to the simultaneous dual integral Eqs. (58)-(60). The representations (54)-(56) ensure that the integral Eqs. (49), (51), and (53) are automatically satisfied, and the integral Eqs. (48), (50), and (52) can be written in the form of the following Abel-type integral Eqs.:

$$\begin{aligned}\int_0^r \frac{d\tilde{\phi}_1(\rho,s)}{d\rho}\frac{d\rho}{\left(r^2-\rho^2\right)^{1/2}} + \int_0^\infty \xi^2\tilde{\tilde{\vartheta}}_{11}(\xi,s)\tilde{\tilde{N}}_1(\xi,s)J_0(\xi r)d\xi + \int_0^\infty \xi^2\tilde{\tilde{\vartheta}}_{12}(\xi,s)\tilde{\tilde{N}}_2(\xi,s)J_0(\xi r)d\xi \\ + \int_0^\infty \xi^2\tilde{\tilde{\vartheta}}_{13}(\xi,s)\tilde{\tilde{N}}_3(\xi,s)J_0(\xi r)d\xi = \sigma/s, \quad ; \quad r<a \ ; \quad \forall t\geq 0\end{aligned} \tag{B.2}$$

$$\int_0^\infty \tilde{\vartheta}_{21}(\xi,s)\tilde{\bar{N}}_1(\xi,s)J_0(\xi r)d\xi + \int_0^r \frac{d\tilde{\phi}_2(\rho,s)}{\left(r^2-\rho^2\right)^{1/2}} + \int_0^\infty \tilde{\vartheta}_{22}(\xi,s)\tilde{\bar{N}}_2(\xi,s)J_0(\xi r)d\xi + \int_0^\infty \tilde{\vartheta}_{22}(\xi,s)\tilde{\bar{N}}_2(\xi,s)J_0(\xi r)d\xi = p/s, \quad ; \quad r<a \ ; \ \forall t \geq 0 \tag{B.3}$$

$$\int_0^\infty \xi^2\tilde{\vartheta}_{31}(\xi,s)\tilde{\bar{N}}_1(\xi,s)J_1(\xi r)d\xi + \int_0^\infty \xi^2\tilde{\vartheta}_{32}(\xi,s)\tilde{\bar{N}}_2(\xi,s)J_1(\xi r)d\xi + \sqrt{\frac{2}{\pi}}\int_0^r \frac{d\left(\sqrt{\rho}\tilde{\phi}_3(\rho,s)\right)}{d\rho}\frac{d\rho}{r\left(r^2-\rho^2\right)^{1/2}} + \int_0^\infty \tilde{\vartheta}_{33}(\xi,s)\tilde{\bar{N}}_3(\xi,s)J_1(\xi r)d\xi = 0. \quad ; \quad r<a \ ; \ \forall t \geq 0 \tag{B.4}$$

The following integrals were used in the derivation of (B.2) - (B.4):

$$\int_0^\infty J_0(\xi r)\cos(\xi\rho)d\xi = \begin{cases} \left(r^2-\rho^2\right)^{-1/2} & ; \quad 0<\rho<r \\ 0 & ; \quad \rho>r \end{cases} \tag{B.5}$$

$$\int_0^\infty J_1(\xi r)\sin(\xi\rho)d\xi = \begin{cases} (\rho/r)\left(r^2-\rho^2\right)^{-1/2} & ; \quad 0<\rho<r \\ 0 & ; \quad \rho>r \end{cases} \tag{B.6}$$

Using the expressions for $\tilde{\bar{N}}_i(\xi,s);\ i=1,\ 2,\ 3,$ (B.2) - (B.4) can be inverted to

$$\begin{aligned} &\tilde{\phi}_1(\rho,s) + \tfrac{2}{\pi}\int_0^\infty \xi^2\tilde{\vartheta}_{11}(\xi,s)\tilde{\bar{N}}_1(\xi,s)\left[\int_0^\rho r\left(\rho^2-r^2\right)^{-1/2}J_0(\xi r)dr\right]d\xi \\ &+\tfrac{2}{\pi}\int_0^\infty \xi^2\tilde{\vartheta}_{12}(\xi,s)\tilde{\bar{N}}_2(\xi,s)\left[\int_0^\rho r\left(\rho^2-r^2\right)^{-1/2}J_0(\xi r)dr\right]d\xi \\ &+\tfrac{2}{\pi}\int_0^\infty \xi^2\tilde{\vartheta}_{13}(\xi,s)\tilde{\bar{N}}_3(\xi,s)\left[\int_0^\rho r\left(\rho^2-r^2\right)^{-1/2}J_0(\xi r)dr\right]d\xi \\ &= \tfrac{2\sigma}{\pi s}\left[\int_0^\rho r\left(\rho^2-r^2\right)^{-1/2}dr\right], \qquad ; \quad r<a \ ; \ \forall t \geq 0 \end{aligned} \tag{B.7}$$

$$\begin{aligned} &\tilde{\phi}_2(\rho,s) + \int_0^\infty \tilde{\vartheta}_{21}(\xi,s)\tilde{\bar{N}}_1(\xi,s)\left[\frac{d}{d\rho}\int_0^\rho r\left(u^2-r^2\right)^{-1/2}J_0(\xi r)dr\right]d\xi \\ &+\int_0^\infty \tilde{\vartheta}_{22}(\xi,s)\tilde{\bar{N}}_2(\xi,s)\left[\frac{d}{d\rho}\int_0^\rho r\left(u^2-r^2\right)^{-1/2}J_0(\xi r)dr\right]d\xi \\ &+\int_0^\infty \tilde{\vartheta}_{22}(\xi,s)\tilde{\bar{N}}_2(\xi,s)\left[\frac{d}{d\rho}\int_0^\rho r\left(u^2-r^2\right)^{-1/2}J_0(\xi r)dr\right]d\xi \\ &= \tfrac{2p}{\pi s}\left[\tfrac{d}{d\rho}\int_0^\rho r\left(\rho^2-r^2\right)^{-1/2}dr\right], \qquad ; \quad r<a \ ; \ \forall t \geq 0 \end{aligned} \tag{B.8}$$

$$\begin{aligned} &\sqrt{\rho}\tilde{\phi}_3(\rho,s) + \sqrt{\tfrac{2}{\pi}}\int_0^\infty \xi^2\tilde{\vartheta}_{31}(\xi,s)\tilde{\bar{N}}_1(\xi,s)\left[\int_0^\rho r^2\left(\rho^2-r^2\right)^{-1/2}J_1(\xi r)\right]d\xi \\ &+\sqrt{\tfrac{2}{\pi}}\int_0^\infty \xi^2\tilde{\vartheta}_{32}(\xi,s)\tilde{\bar{N}}_2(\xi,s)\left[\int_0^\rho r^2\left(\rho^2-r^2\right)^{-1/2}J_1(\xi r)\right]d\xi \\ &+\sqrt{\tfrac{2}{\pi}}\int_0^\infty \tilde{\vartheta}_{33}(\xi,s)\tilde{\bar{N}}_3(\xi,s)\left[\int_0^\rho r^2\left(\rho^2-r^2\right)^{-1/2}J_1(\xi r)\right]d\xi = 0. \quad ; \quad r<a \ ; \ \forall t \geq 0 \end{aligned} \tag{B.9}$$

With the aid of the results

$$\int_0^\rho r\left(\rho^2-r^2\right)^{-1/2}J_0(\xi r)dr = \xi^{-1}\sin(\xi\rho), \tag{B.10}$$

$$\int_0^\rho r\left(\rho^2 - r^2\right)^{-1/2} dr = \rho, \tag{B.11}$$

$$\int_0^\rho r^2\left(\rho^2 - r^2\right)^{-1/2} J_1(\xi r) dr = \sqrt{\frac{\pi}{2\xi}}\rho^{3/2} J_{3/2}(\xi\rho). \tag{B.12}$$

Eqs. (B.7)–(B.9) can be written in the form of the system of Fredholm integral equations of the second kind given in (57)–(59). The Kernel functions in these equations can be written as:

$$\tilde{\Omega}_{11}(r,\rho,s) = \frac{2}{\pi}\int_0^\infty \tilde{\tilde{\vartheta}}_{11}(\xi,s)\sin(\xi r)\sin(\xi\rho)d\xi, \tag{B.13}$$

$$\tilde{\Omega}_{12}(r,\rho,s) = \frac{2}{\pi}\int_0^\infty \xi\tilde{\tilde{\vartheta}}_{12}(\xi,s)\sin(\xi r)\cos(\xi\rho)d\xi, \tag{B.14}$$

$$\tilde{\Omega}_{13}(r,\rho,s) = \frac{2}{\pi}\int_0^\infty \sqrt{\xi}\tilde{\tilde{\vartheta}}_{13}(\xi,s)\sin(\xi r)J_{3/2}(\xi\rho)d\xi, \tag{B.15}$$

$$\tilde{\Omega}_{21}(r,\rho,s) = \frac{2}{\pi}\int_0^\infty \frac{1}{\xi}\tilde{\tilde{\vartheta}}_{21}(\xi,s)\cos(\xi r)\sin(\xi\rho)d\xi, \tag{B.16}$$

$$\tilde{\Omega}_{22}(r,\rho,s) = \frac{2}{\pi}\int_0^\infty \tilde{\tilde{\vartheta}}_{22}(\xi,s)\cos(\xi r)\cos(\xi\rho)d\xi, \tag{B.17}$$

$$\tilde{\Omega}_{23}(r,\rho,s) = \frac{2}{\pi}\int_0^\infty \frac{1}{\sqrt{\xi}}\tilde{\tilde{\vartheta}}_{23}(\xi,s)\cos(\xi r)J_{3/2}(\xi\rho)d\xi, \tag{B.18}$$

$$\tilde{\Omega}_{31}(r,\rho,s) = r\int_0^\infty \sqrt{\xi}\tilde{\tilde{\vartheta}}_{31}(\xi,s)J_{3/2}(\xi r)\sin(\xi\rho)d\xi, \tag{B.19}$$

$$\tilde{\Omega}_{32}(r,\rho,s) = r\int_0^\infty \xi^{3/2}\tilde{\tilde{\vartheta}}_{12}(\xi,s)J_{3/2}(\xi r)\cos(\xi\rho)d\xi, \tag{B.20}$$

$$\tilde{\Omega}_{33}(r,\rho,s) = r\int_0^\infty \xi\tilde{\tilde{\vartheta}}_{33}(\xi,s)J_{3/2}(\xi r)J_{3/2}(\xi\rho)d\xi. \tag{B.21}$$

The expressions for the functions $\tilde{\tilde{\vartheta}}_{ij}(\xi,s)\ ;\ i,j = 1-3$ can be found in the website.

The axial and shear stresses at the injection plane $z = 0$, can be written as

$$\tilde{\sigma}_{zz}^{(L)}(r,0,s) = \int_0^\infty \xi^2\left\{\left(\tilde{\tilde{\vartheta}}_{11}+1\right)\tilde{\tilde{N}}_1(\xi,s) + \tilde{\tilde{\vartheta}}_{12}\tilde{\tilde{N}}_2(\xi,s) + \tilde{\tilde{\vartheta}}_{13}\tilde{\tilde{N}}_3(\xi,s)\right\}J_0(\xi r)d\xi \quad ; \quad r < a \quad ; \quad \forall t \geq 0 \tag{B.22}$$

$$\tilde{\sigma}_{rz}^{(L)}(r,0,s) = \int_0^\infty \xi^2\left\{\tilde{\tilde{\vartheta}}_{31}\tilde{\tilde{N}}_1(\xi,s) + \tilde{\tilde{\vartheta}}_{32}\tilde{\tilde{N}}_2(\xi,s) + \left(\tilde{\tilde{\vartheta}}_{33}+1\right)\tilde{\tilde{N}}_3(\xi,s)\right\}J_1(\xi r)d\xi \quad ; \quad r < a \quad ; \quad \forall t \geq 0 \tag{B.23}$$

Using the expressions for $\tilde{\tilde{N}}_i(\xi,s);\ i = 1,\ 2,\ 3$ and relations (B.5) and (B.6), (B.22) and (B.23) can be further reduced to the following form

$$\tilde{\sigma}_{zz}^{(L)}(r,0,s) = -\frac{\tilde{\phi}_1(a,s)}{\sqrt{r^2-a^2}} \quad ; \quad r < a \quad ; \quad \forall t \geq 0 \tag{B.24}$$

$$\tilde{\sigma}_{rz}^{(L)}(r,0,s) = -\sqrt{\frac{2a}{\pi}}\frac{\tilde{\phi}_3(a,s)}{r\sqrt{r^2-a^2}} \quad ; \quad r < a \quad ; \quad \forall t \geq 0 \tag{B.25}$$

The expressions for the Mode I and Mode II stress intensity factors, for loading cases 1 and 2, can thus be given by the limits (60) and (61).

The crack opening displacement can be found by substituting the unknow functions $A_1^{(L)}, B_1^{(L)}, \ldots, A_3^{(H)}$ in (37)-(40) and the transform expression for $u_z^{(m)}(r,0,t)\ ;\ m = \mathrm{L,H}$ in (14). Thus, the expression for the crack opening displacement corresponding to the Layer and the halfspace regions can be obtained as:

$$\begin{aligned}\tilde{u}_z^{(m)}(r,0,s) = \int_0^\infty \xi\Big[&\tilde{\upsilon}_1^{(m)}(\xi,s)\tilde{\tilde{N}}_1(\xi,s) + \tilde{\upsilon}_2^{(m)}(\xi,s)\tilde{\tilde{N}}_2(\xi,s) \\ &+\tilde{\upsilon}_3^{(m)}(\xi,s)\tilde{\tilde{N}}_3(\xi,s)\Big]J_0(\xi r)d\xi \quad ; \quad r < a \quad ; \quad m = \mathrm{L,H}\end{aligned} \tag{B.26}$$

where the functions $\tilde{\upsilon}_i^{(m)}(\xi, s)$; $i = 1 - 3$; $m = \mathrm{L}, \mathrm{H}$ can be found in the website.

Using the representations for $\tilde{\bar{N}}_i(\xi, s)$; $i = 1,\ 2,\ 3$ in (B.26), $\tilde{u}_z^{(\mathrm{L})}(r, 0, s)$ can be written in terms of $\tilde{\phi}_1(\rho, s)$, $\tilde{\phi}_2(\rho, s)$, and $\tilde{\phi}_3(\rho, s)$ as:

$$\tilde{u}_z^{(m)}(r, 0, s) = \int_0^a \Big[\tilde{\phi}_1(\rho, s)\tilde{\omega}_1^{(m)}(r, \rho, s) + \tilde{\phi}_2(\rho, s)\tilde{\omega}_2^{(m)}(r, \rho, s) + \tilde{\phi}_3(\rho, s)\tilde{\omega}_3^{(m)}(r, \rho, s)\Big] d\rho \quad ; \quad r < a \ ; \ m = \mathrm{L}, \mathrm{H} \tag{B.27}$$

where

$$\tilde{\omega}_1^{(m)}(r, \rho, s) = \int_0^\infty \tilde{\upsilon}_1^{(m)}(\xi, s) \sin(\xi\rho) J_0(\xi r) d\xi \quad ; \quad m = \mathrm{L}, \mathrm{H} \tag{B.28}$$

$$\tilde{\omega}_2^{(m)}(r, \rho, s) = \int_0^\infty \xi\tilde{\upsilon}_2^{(m)}(\xi, s) \cos(\xi\rho) J_0(\xi r) d\xi \quad ; \quad m = \mathrm{L}, \mathrm{H} \tag{B.29}$$

$$\tilde{\omega}_3^{(m)}(r, \rho, s) = \int_0^\infty \xi^{1/2}\tilde{\upsilon}_3^{(m)}(\xi, s) J_{3/2}(\xi\rho) J_0(\xi r) d\xi \quad ; \quad m = \mathrm{L}, \mathrm{H} \tag{B.30}$$

Thus, the crack volume for both loading cases can be obtained by integrating the relation for the crack opening displacements (B.27) along the crack face $(0, a)$ as in (62).

References

Aadnoy, B., & Looyeh, R. (2019). *Petroleum rock mechanics: Drilling operations and well design*. Gulf Professional Publishing.

Abousleiman, Y., Cheng, A. H.-D., Cui, L., Detournay, E., & Roegiers, J.-C. (1996). Mandel's problem revisited. *Géotechnique, 46*, 187–195.

Adachi, J. I., & Detournay, E. (2008). Plane strain propagation of a hydraulic fracture in a permeable rock. *Engineering Fracture Mechanics, 75*, 4666–4694.

Aliabadi, M. H. (1997). Boundary element formulations in fracture mechanics. *Applied Mechanics Reviews, 50*, 83–96.

Altay, G. A., & Dökmeci, M. C. (1998), *A uniqueness theorem in Biot's poroelasticity theory* (49, pp. 838–846). Zeitschrift für angewandte Mathematik und Physik ZAMP.

Atkinson, B. K. (1984). Subcritical crack growth in geological materials. *Journal of Geophysical Research: Solid Earth, 89*(B6), 4077–4114.

Atkinson, C. (1979). Stress singularities in fracture mechanics. *Applied Mechanics Reviews, 32*, 123–135.

Atkinson, C., & Craster, R. V. (1991). Plane strain fracture in poroelastic media. *Proceedings of the Royal Society of London. Series A, 434*, 605–633.

Atkinson, C., & Craster, R. V. (1995). Theoretical aspects of fracture mechanics. *Progress in Aerospace Science, 31*, 1–83.

Barenblatt, G. I. (1956). On certain problems of the theory of elasticity that arise in the investigation of the mechanism of hydraulic rupture of an oil-bearing layer. *Prikladnaia Matematika i Mehanika Akademii Nauk, 20*, 475–486.

Barenblatt, G. I. (1957). An approximate evaluation of the size of a crack forming in hydraulic fracture of a stratum. *Izvestia Akademii Nauk, 3*, 1980–1982.

Barenblatt, G. I. (1959). Equilibrium cracks forming during brittle fracture. *Doklady. Akadamii Nauk, 127*, 1980–1982.

Barenblatt, G. I. (1962). The mathematical theory of equilibrium cracks in brittle fracture. *Advances in Applied Mechanics, 7*, 55–129.

Barsoum, R. S. (1976). On the use of isoparametric finite elements in linear fracture mechanics. *International Journal for Numerical Methods in Engineering, 10*(1), 25–37.

Bazant, Z. P. (1981). Anelasticity and fracture of concrete. Mechanics of Structured Media Part B, *(A.P.S. Selvadurai, Ed.)* Studies in Applied Mechanics 5B (pp. 3–35). Amstredam. Elsevier Scientific Publishing Co.

Bazant, Z. P., & Planas, J. (1998). *Fracture and size effect in concrete and other quasi-brittle materials*. Boca Raton, FL: CRC press.

Benz, T., & Schwab, R. (2008). A quantitative comparison of six rock failure criteria. *International Journal of Rock Mechanics and Mining Sciences, 45*(7), 1176–1186.

Biot, M. A. (1941). General theory of three-dimensional consolidation. *Journal of Applied Physics, 12*, 155–164.

Biot, M. A. (1956). General solutions of the equations of elasticity and consolidation for a porous material. *Journal of Applied Mechanics, 23*, 91–96.

Brace, W. F., & Bombalakis, E. G. (1963). A note on brittle crack growth in compression. *Journal of Geophysical Research, 68*, 3709–3713.

Brace, W. F. (1960). An extension of the Griffith theory of fracture to rocks. *Journal of Geophysical Research, 65*, 3477–3480.

Bradley, W. B. (1979). Failure of inclined boreholes. *Journal of Energy Resources Technology, 101*, 232–239.

Broberg, B. K. (1999). *Cracks and fracture*. San Diego, California: Academic Press.

Broek, D. (1982). *Elementary fracture mechanics*. The Hague, Netherlands: Martinus Nijhoff Publishers.

Chan, S. K., Tuba, I. S., & Wilson, W. K. (1970). On the finite element method in linear fracture mechanics. *Engineering Fracture Mechanics, 2*, 1–17.

Chan, T., & Stanchell, F. W. (2009). Implications of glaciation and coupled thermo-hydro-mechanical processes on shield flow system evolution and performance assessment. *Environmental Geology, 57*, 1371–1389.

Chau, V. T., Bažant, Z. P., & Su, Y. (2016). Growth model for large branched three-dimensional hydraulic crack system in gas or oil shale. *Philosophical Transactions of the Royal Society A, 374*, Article 20150418.

Chen, W. F., & Baladi, G. (1985). *Soil plasticity: Theory and implementation*. New York: Elsevier Science Publishers B.V..

Cheng, A. H. (1987). Transient boundary element formulation for linear poroelasticity. *Applied Mathematical Modeling, 11*, 285–290.

Cheng, A. H. (1993). Review of some poroelastic effects in rock mechanics. *International Journal of Rock Mechanics and Mining Sciences. Geomechanics Abstracts, 30*(7), 1119–1126 Pergamon.

Cheng, A. H. (1994). Approximate inversion of the Laplace transform. *Mathematica Journal, 4*, 76–82.

Cheng, A. H. (2016). *D.* Poroelasticity *(Vol. 27)*. Switzerland: Springer International Publishing.

Cherepanov, G. P. (1979). *Mechanics of brittle fracture*. New York: McGraw-Hill R., de Wit & W. C., Cooley (Eds.).

Cherepanov, G. P. (2015). The mechanics and physics of fracturing: Applications to thermal aspects of crack propagation and to fracking. *Philosophical Transactions of the Royal Society A, 373*, Article 20140119.

Cleary, M. P. (1977). Fundamental solutions for a fluid-saturated porous solid. *International Journal of Solids and Structures, 13*, 785–806.

Cleary, M. P. (1979). Rate and structure sensitivity in hydraulic fracturing of fluid-saturated porous formations. In *Proceedings of 20th US Symposium on Rock Mechanics (USRMS)*. American Rock Mechanics Association.

Cleary, M. P. (1980). Comprehensive design formulae for hydraulic fracturing. In *SPE Annual Technical Conference and Exhibition*. Society of Petroleum Engineers.

Clifton, R., & Abou-Sayed, A. (1979). On the computation of the three-dimensional geometry of hydraulic fractures. In *Symposium on Low Permeability Gas Reservoirs*. Society of Petroleum Engineers.

Cohen, A. M. (2007). *Numerical methods for laplace transform inversion*. Berlin: Springer Science & Business Media.
Copson, E. T. (1961). On certain dual integral equations. *Glasgow Mathematics Journal, 5*, 21–24.
Cottrell, A. H. (1965). Mechanics of fracture in large structures. *Proceedings of the Royal Society of London, Series A, 285*, 10–21.
Craster, R. V., & Atkinson, C. (1996). On finite-length cracks and inclusions in poroelasticity. *The Quarterly Journal of Mechanics and Applied Mathematics, 49*, 311–335.
Cryer, R. W. (1963). A comparison of three-dimensional theories of Biot and Terzaghi. *Quarterly Journal of Mechanics and Applied Mathematics, 16*, 401–412.
Csati, Z., Moës, N., & Massart, T. J. (2020). A stable extended/generalized finite element method with Lagrange multipliers and explicit damage update for distributed cracking in cohesive materials. *Computer Methods in Applied Mechanics and Engineering, 369*, Article 113173.
Cui, L., Abousleiman, Y., Cheng, A. H.-D., & Roegiers, J. C. (1999). Time-dependent failure analysis of inclined boreholes in fluid-saturated formations. *Journal of Energy Resources Technology, 121*, 31–39.
Daneshy, A. A. (1973). On the design of vertical hydraulic fractures. *Journal of Petroleum Technology, 25*, 83–97 *Transactions AIME*.
Daneshy, A. A. (1978). Hydraulic fracture propagation in layered formations. *Society of Petroleum Engineers Journal, 18*, 33–41.
Dargush, G. F., & Banerjee, P. K. (1991). A new boundary element method for three-dimensional coupled problems of consolidation and thermoelasticity. *Journal of Applied Mechanics, 58*, 28–36.
Darve, F. (1990). *Geomaterials: Constitutive equations and modelling*. The Netherlands: Elsevier Applied Science.
Davis, R. O., & Selvadurai, A. P. S. (2005). *Plasticity and geomechanics*. Cambridge University Press.
De Borst, R., Réthoré, J., & Abellan, M. A. (2006). A numerical approach for arbitrary cracks in a fluid-saturated medium. *Archive of Applied Mechanics, 75*, 595–606.
De Josselin de Jong, G. (1953). Consolidation around pore pressure meters. *Journal of Applied Physics, 24*, 922–928.
De Josselin de Jong, G. (1957). Application of stress functions to consolidation problems. In *Proceedings of the 4th International Conference on Soil Mechanics and Foundation Engineering: 1* (pp. 320–323). London.
Desai, C. S., & Siriwardane, H. J. (1984). *Constitutive laws for engineering materials with emphasis on geologic materials*. Englewood Cliffs, NJ: Prentice-Hall.
Desroches, J., Detournay, E., Lenoach, B., Papanastisiou, P., Pearson, J. R. A., Thiercelin, M., & Cheng, A. H.-D. (1994). The crack tip region in hydraulic fracturing. *Proceedings of the Royal Society A, 447*, 39–48.
Detournay, E., & Cheng, A. H. (1989). Poroelasticity considerations in *in situ* stress determination by hydraulic fracturing. *International Journal of Rock Mechanics and Mining Science & Geomechanics Abstracts, 26*, 507–513.
Detournay, E., & Cheng, A. H.-D. (1991). Plane strain analysis of a stationary hydraulic fracture in a poroelastic medium. *International Journal of Solids and Structures, 27*, 1645–1662.
Dong, L., & Atluri, S. N. (2013a). Fracture and fatigue analyses: SGBEM-FEM or XFEM? Part 1: 2D Structures. *Computer Modeling in Engineering and Science, 90*, 91–146.
Dong, L., & Atluri, S. N. (2013b). Fracture and fatigue analyses: SGBEM-FEM or XFEM? Part 2: 3D Solids. *Computer Modeling in Engineering and Science, 90*, 379–413.
Drucker, D. C., & Prager, W. (1952). Soil mechanics and plastic analysis or limit design. *Quarterly of Applied Mathematics, 10*, 157–165.
Elfgren, L. (1989). *RILEM Report*. London: Chapman and Hall.
Ellsworth, D., Voight, B., Ouyang, Z., & Piggott, A. R. (1996). Poroelastic response resulting from magma intrusion. *Mechanics of poroelastic media* (pp. 215–233). Dordrecht, The Netherlands: Kluwer Academic Publishers Selvadurai Ed, A. P. S..
Eshelby, J. D. (1957). The determination of the elastic field of an ellipsoidal inclusion, and related problems. *Proceedings of the Royal Society of London, Series A, 241*, 376–396.
Francis, E. C., Carlton, C. H., & Thompson, R. E. (1974). Viscoelastic rocket grain fracture analysis. *International Journal of Fracture, 10*, 167–180.
Geertsma, J., & Haafkens, R. (1979). Comparison of the theories for predicting width and extent of vertical hydraulically induced fractures. *Journal of Energy Resources Technology, 101*, 8–19.
Gibson, R. E., Knight, K., & Taylor, P. W. (1963). A critical experiment to examine theories of three-dimensional consolidation. *P*roceedings of the European Conference on Soil Mechanics and Foundation Engineering, *1*, 69–76.
Głowacki, A., & Selvadurai, A. P. S. (2016). Stress-induced permeability changes in Indiana limestone. *Engineering Geology, 215*, 122–130.
Goodier, J. N. (1933). Concentration of stress around spherical and cylindrical inclusions and flaws. *Transactions of the American Society of Mechanical Engineering, 55*, 39–44.
Griffith, A. A. (1921). The phenomenon of rupture and flow in solids. *Philosophical Transactions of the Royal Society of London. Series A, 221*, 163–168.
Griffith, A. A. (1924). The theory of rupture. *1st international congress on applied mechanics* (pp. 55–63) Delft.
Guéguen, Y., & Kachanov, M. (2011). Effective elastic properties of cracked rocks-An overview. *Mechanics of Crustal Rocks* (pp. 73–125). Vienna: Springer.
Guz, A. N., Bogdanov, V. L., & Nazarenko, V. M. (2020). Fracture of materials under compression along cracks. *Advanced Structural Materials Series*.
Guz, A. N., & Nazarenko, V. M. (1985). Symmetric failure of the halfspace with penny-shaped cracks in compression. *Theoretical and Applied Fracture Mechanics, 3*, 233–245.
Hart, D. J., & Wang, H. F. (1995). Laboratory measurements of a complete set of poroelastic moduli for Berea sandstone and Indiana limestone. *Journal of Geophysical Research: Solid Earth, 100*, 17741–17751.
Hellan, K. (1985). *Introduction to fracture mechanics*. New York: McGraw-Hill.
Hills, D. A., Kelly, P. A., Dai, D. N., & Korsunsky, A. M. (1996). *Solution of crack problems*: *The distributed dislocation technique*. *Solid mechanics and its applications series*.
Hoek, E., & Brown, E. T. (2019). The Hoek–Brown failure criterion and GSI–2018 edition. *Journal of Rock Mechanics and Geotechnical Engineering, 11*, 445–463.
Holzbecher, E. (2016). Multiphysics modelling of the Mandel-Cryer effect. *International Journal of Multiphysics, 10*, 11–20.
Hossain, M. M., Rahman, M. K., & Rahman, S. S. (2000). Hydraulic fracture initiation and propagation: Roles of wellbore trajectory, perforation and stress regimes. *Journal of Petroleum Science and Engineering, 27*, 129–149.
Howard, G. C., & Fast, C. R. (1970). Hydraulic fracturing, monograph series. *Society of Petroleum Engineering AIME, 2*, 34 Richardson, TX.
Hu, J., & Garagash, D. I. (2010). Plane-strain propagation of a fluid-driven crack in a permeable rock with fracture toughness. *Journal of Engineering Mechanics, 136*, 1152–1166.
Huang, J., Griffiths, D. V., & Wong, S. W. (2012). Initiation pressure, location and orientation of hydraulic fracture. *International Journal of Rock Mechanics and Mining Sciences, 49*, 59–67.
Inglis, C. E. (1913). Stresses in a plate due to the presence of cracks and sharp corners. *Transactions of the Royal Institute of Naval Architects, 55*, 219–241.
Jaeger, Ch. (1972). *Rock mechanics and engineering*. Cambridge: Cambridge University Press.
Jaeger, J. C. (1971). Friction of rocks and stability of rock slopes. *Geotechnique, 21*, 97–134.
Jaeger, J. C., Cook, N. G. W., & Zimmermann, R. (2007). *Fundamentals of rock mechanics*. New York: John Wiley.
Jiang, H., & Xie, Y. (2011). A note on the Mohr–Coulomb and Drucker–Prager strength criteria. *Mechanics Research Communications, 38*, 309–314.
Jin, B., & Zhong, Z. (2002). Dynamic stress intensity factor (Mode I) of a penny-shaped crack in an infinite poroelastic solid. *International Journal of Engineering Science, 40*, 637–646.
Kachanov, M. L. (1992). Effective elastic properties of cracked solids: Critical review of some concepts. *Applied Mechanics Reviews, 45*, 304–335.
Kachanov, M. L., Shafiro, B., & Tsukrov, I. (2013). *Handbook of elasticity solutions*. Springer Science & Business Media.
Kanin, E. A., Garagash, D. I., & Osiptsov, A. A. (2020). The near-tip region of a hydraulic fracture with pressure-dependent leak-off and leak-in. *Journal of Fluid Mechanics*, 892.
Karihaloo, B. (1995). Fracture mechanics and structural concrete, *longman scientific and technical*. Burnt Mill, Harlow.
Kassir, M. K., & Sih, G. C. (1975). Three-dimensional crack problems. *Mechanics of fracture 2*. Leyden: Noordhoff International Publishers G. C., Sih (Ed.).

Khalili, N., & Selvadurai, A. P. S. (2003). A fully coupled constitutive model for thermo-hydro-mechanical analysis in elastic media with double porosity. *Geophysical Research Letters*, 30.
Khristianovitch, S. A., & Zheltov, Y. P. (1955). Formation of vertical fractures by means of highly viscous fluids. In *Proceedings 4th World Petroleum Congress* (pp. 579–586). Rome, Italy. *2*.
Kim, J., & Selvadurai, A. P. S. (2015). Ground heave due to line injection sources. *Geomechanics for Energy and the Environment, 2*, 1–14.
Knauss, W. G. (1970). Delayed failure-the griffith problem for linearly viscoelastic materials. *International Journal of Fracture Mechanics, 6*, 7–20.
Kolosov, G. V. (1935). *Application of complex diagrams and the theory of complex variables to the theory of elasticity*. Moscow: ONTI.
Krajcinovic, D. (1984). Continuous damage mechanics. *Applied Mechanics Reviews, 37*, 1–6.
Lawn, B. R., & Wilshaw, T. R. (1975). *Fracture of brittle solids*. Cambridge, UK: Cambridge University Press.
Le Tirant, P., & Dupuy, M. (1967). Dimensions of the fractures obtained by hydraulic fracturing of oil-bearing formations. In *Revue de l'Institut Francois du Petrole* (pp. 44–98).
Lecampion, B., Bunger, A., & Zhang, X. (2018). Numerical methods for hydraulic fracture propagation: A review of recent trends. *Journal of Natural Gas Science and Engineering, 49*, 66–83.
Lee, J. L., Mardal, K. A., & Winther, R. (2017). Parameter-robust discretization and preconditioning of Biot's consolidation model. *SIAM Journal of Scientific Computing, 39*, A1–A24.
Liebowitz, H. (1968). Fracture, and advanced treatise. *Vol. I-IV*. New York: Academic Press.
Ma, Y. Z., & Holditch, S. A. (2016). *Unconventional oil and gas resources handbook: Evaluation and development*. Amsterdam: Elsevier.
Mader, D. (1989). *Hydraulic proppant fracturing and gravel packing*. Amsterdam: Elsevier.
Maier, G., Bocciarelli, M., Bolzon, G., & Fedele, R. (2006). Inverse analysis in fracture mechanics. *International Journal of Fracture, 138*, 47–73.
Mandel, J. (1953). Consolidation des sols (etude mathématique). *Géotechnique, 3*, 287–299.
Massart, T. J., & Selvadurai, A. P. S. (2012). Stress-induced permeability evolution in a quasi-brittle geomaterial. *Journal of Geophysical Research, Solid Earth*, (B7), 117.
Massart, T. J., & Selvadurai, A. P. S. (2014). Computational modelling of crack-induced permeability evolution in granite with dilatant cracks. *International Journal of Rock Mechanics and Mining Sciences, 70*, 593–604.
McClintock, F. A., & Walsh, J. (1962). Friction on Griffith's cracks in rock under pressure. *Proc. 4th US National Congress on Applied Mechanics, 2*, 1015–1022.
McNamee, J., & Gibson, R. E. (1960a). Displacement functions and linear transforms applied to diffusion through porous elastic media. *The Quarterly Journal of Mechanics and Applied Mathematics, 13*, 98–111.
McNamee, J., & Gibson, R. E. (1960b). Plane strain and axially symmetric problems of consolidation of a semi-infinite clay stratum. *The Quarterly Journal of Mechanics and Applied Mathematics, 13*, 210–227.
McTigue, D. F. (1986). Thermoelastic response of fluid-saturated porous rock. *Journal of Geophysical Research: Solid Earth, 91*, 9533–9542.
Mendelsohn, D. A. (1984a). A review of hydraulic fracture modeling- ii: 3D modeling and vertical growth in layered rock. *Journal of Energy Resources Technology, 106*, 543–553.
Mendelsohn, D. A. (1984b). A review of hydraulic fracturing modeling- i: General concepts, 2D models, motivation for 3D modeling. *Journal of Energy Resources Technology, 106*, 369–376.
Miehe, C., & Mauthe, S. (2016). Phase field modeling of fracture in multi-physics problems. Part III. Crack driving forces in hydro-poro-elasticity and hydraulic fracturing of fluid-saturated porous media. *Computer Methods in Applied Mechanics and Engineering, 304*, 619–655.
Moës, N., & Belytschko, T. (2002). Extended finite element method for cohesive crack growth. *Engineering Fracture Mechanics, 69*, Article 8130833.
Moës, N., Dolbow, J., & Belytschko, T. (1999). A finite element method for crack growth without re-meshing. *International Journal for Numerical Methods in Engineering, 46*, 131–150.
Murrell, S. A. F. (1962). The effect of high pressure on brittle fracture. In *Proc. Conf Phys. Chem. High Pressure*. London.
Muskhelishvili, N. I. (1953). *Some basic problems of the mathematical theory of elasticity*. Groningen: Noordhoff International Publishers.
Najari, M., & Selvadurai, A. P. S. (2014). Thermo-hydro-mechanical response of granite to temperature changes. *Environmental Earth Sciences, 72*, 189–198.
Nemat-Nasser, S., Abé, H., & Hirakawa, S. (1983). Hydraulic fracturing and geothermal energy. In *Proceedings of the 1st Japan-USA Joint Seminar on Hydraulic Fracturing and Geothermal Energy*. The Hague: Martinus-Nijhoff Publishers.
Nordgren, R. P. (1972). Propagation of a vertical hydraulic fracture. *Society of Petroleum Engineering Journal, 12*, 306–314.
Pande, G. N., Beer, G., & Williams, J. R. (1990). *Numerical methods in rock mechanics*. Chichester, UK: John Wiley.
Pariseau, W. G. (1999). Poroelastic-plastic consolidation-analytical solution. *International Journal for Numerical and Analytical Methods Geomechanics, 23*, 577–594.
Parks, D. M. (1974). A stiffness derivative finite element technique for determination of crack tip stress intensity factors. *International Journal of Fracture, 10*, 487–502.
Peng, J., Rong, G., Cai, M., Wang, X. J., & Zhou, C. B. (2014). An empirical failure criterion for tight rocks. *Rock Mechanics and Rock Engineering, 47*, 347–356.
Perkins, T. K., & Kern, L. R. (1961). Widths of hydraulic fractures. *Journal of Petroleum Technology, 13*, 937–949.
Pietruszczak, S. (2010). *Fundamentals of plasticity in geomechanics*. Boca Raton, FL: CRC Press.
Popelar, C. H., & Kanninen, M. F. (1985). Advanced fracture mechanics. Oxford engineering science series *(Vol 15)*. Oxford: Oxford University Press.
Rahimi, R., & Nygaard, R. (2015). Comparison of rock failure criteria in predicting borehole shear failure. *International Journal of Rock Mechanics and Mining Sciences, 79*, 29–40.
Rajapakse, R. K. N. D., & Senjuntichai, T. (1993). Fundamental solutions for a poroelastic half-space with compressible constituents. *Journal of Applied Mechanics, 60*, 847–856.
Rajapakse, R. K. N. D., & Senjuntichai, T. (1995). An indirect boundary integral equation method for poroelasticity. *International Journal for Numerical and Analytical Methods and Geomechanics, 19*, 587–614.
Réthoré, J., de Borst, R., & Abellan, M. A. (2007). A two-scale approach for fluid flow in fractured porous media. *International Journal for Numerical Methods in Engineering, 71*, 780–800.
Rice, J. R. (1968). A path independent integral and the approximate analysis of strain concentration by notches and cracks. *Journal of Applied Mechanics, 35*, 379–386.
Rice, J. R., & Cleary, M. P. (1976). Some basic stress diffusion solutions for fluid-saturated elastic porous media with compressible constituents. *Reviews of Geophysics, 14*, 227–241.
Rice, J. R., & Simons, D. A. (1976). The stabilization of spreading shear faults by coupled deformation-diffusion effects in fluid-infiltrated porous materials. *Journal of Geophysical Research, 81*, 5322–5334.
Rossmanith, H. P. (1983). Modelling of fracture process zones and singularity dominated zones. *Engineering Fracture Mechanics, 17*, 509–525.
Rudnicki, J. W. (1980). Fracture mechanics applied to the earth's crust. *Annual Review of Earth Planetary Sciences, 8*, 489–525.
Rudnicki, J. W. (1984). Effects of dilatant hardening on the development of concentrated shear deformation in fissured rock masses. *Journal of Geophysical Research, 89*, 9259–9270.
Rudnicki, J. W. (1996). Moving and stationary dislocations in poroelastic solids and applications to aseismic slip in poroelastic solids and applications to aseismic slip in the earth's crust. *Mechanics of poroelastic media* (pp. 3–22). Dordrecht, The Netherlands: Kluwer Academic Publishers A.P.S.Selvadurai, Ed..
Rudnicki, J. W., & Roeloffs, E. A. (1990). Plane strain shear dislocations moving steadily in linear elastic diffusive solids. *Journal of Applied Mechanics, 57*, 32–39.
Rutqvist, J., & Tsang, C. F. (2002). A study of caprock hydromechanical changes associated with CO2 injection into a brine formation. *Environmental Geology, 42*, 296–305.

Rybicki, E. F., & Kanninen, M. F. (1977). A finite element calculation of stress intensity factors by a modified crack closure integral. *Engineering Fracture Mechanics, 9*, 931–938.
Salimzadeh, S., Paluszny, A., & Zimmerman, R. W. (2017). Three-dimensional poroelastic effects during hydraulic fracturing in permeable rocks. *International Journal of Solids and Structures, 108*, 153–163.
Samea, P., & Selvadurai, A. P. S. (2020). A contact problem for a poroelastic halfspace containing an embedded inextensible membrane. *International Journal for Numerical and Analytical Methods in Geomechanics, 44*, 2167–2188.
Sandhu, R. S., & Wilson, E. L. (1969). Finite-element analysis of seepage in elastic media. *Journal of Engineering Mechanics, 95*, 641–652.
Sanford, R. J. (1997). *Selected papers on foundations of linear elastic fracture mechanics*. SPIE Press Vol. MS 137SC.
Savitski, A. A., & Detournay, E. (2002). Propagation of a penny-shaped fluid-driven fracture in an impermeable rock: Asymptotic solutions. *International Journal of solids and Structures, 39*, 6311–6337.
Schapery, R. A. (1962). Approximation methods of transform inversion for viscoelastic stress analysis. In *Proceedings of the 4th US national congress on applied mechanics* (pp. 1075–1085). New York.
Schapery, R. A. (1975). A theory of crack initiation and growth in viscoelastic media-I. Theoretical development. *International Journal of Fracture, 1*, 141–159.
Schofield, A. N., & Wroth, C. P. (1968). *Critical state soil mechanics*. McGraw-Hill, London.
Selvadurai, A. P. S. (2007). The analytical method in geomechanics. *Applied Mechanics Reviews, 60*, 87–106.
Selvadurai, A. P. S. (1980). The penny-shaped crack problem for a finitely deformed incompressible elastic solid. *International Journal of Fracture, 16*, 327–333.
Selvadurai, A. P. S. (1992). Transient thermoviscoelastic response of a crack in a layered structure. *Journal of Thermal Stresses, 15*, 143–167.
Selvadurai, A. P. S. (2000). Fracture evolution during indentation of a brittle elastic solid. *Mechanics of Cohesive-Frictional Materials, 5*, 325–339.
Selvadurai, A. P. S. (2006). Non-linear mechanics of cracks subjected to indentation. *Canadian Journal of Civil Engineering, 33*, 766–775.
Selvadurai, A. P. S. (2009). Heave of a surficial rock layer due to pressure, generated by injection fluids. *Geophysical Research Letters, 36*, L14302. https://doi.org/10.1029/2009GL038187.
Selvadurai, A. P. S. (2012). A geophysical application of an elastostatic contact problem. *Mathematics and Mechanics of Solids, 18*, 192–207.
Selvadurai, A. P. S. (2019a). Proppant-induced opening of hydraulically created fractures. *Open Geomechanics, 1*, 1–10.
Selvadurai, A. P. S. (2019b). The Biot coefficient for a low permeability heterogeneous limestone. *Continuum Mechanics and Thermodynamics, 31*, 939–953.
Selvadurai, A. P. S. (2020). In-plane loading of a bonded rigid inclusion embedded at a pre-compressed elastic interface: The role of non-linear interface responses. *Mechanical systems and signal processing*: 144.
Selvadurai, A. P. S. (2021). Irreversibility of soil skeletal deformations: The pedagogical limitations of Terzaghi's celebrated model for soil consolidation. Computers and Geotechnics *(Accepted)*. https://doi.org/10.1016/j.compgeo.2021.104137.
Selvadurai, A. P. S., Suvorov, A. P., & Selvadurai, P. A. (2015). Thermo-hydro-mechanical processes in fractured rock formations during a glacial advance. *Geoscientific Model Development, 8*, 2167–2185.
Selvadurai, A. P. S. (Ed.). (2013). Mechanics of poroelastic media *(Vol. 35)*. Springer Science & Business Media.
Selvadurai, A. P. S., Au, M. C., & Phang, W. A. (1990). Modelling of low temperature behaviour of cracks in asphaltic pavement structures. *Canadian Journal of Civil Engineering, 17*, 844–858.
Selvadurai, A. P. S., & Busschen, ten A. (1995). Mechanics of segmentation of an embedded fiber, Part II: Computational modeling and comparisons. *Journal of Applied Mechanics, 62*, 98–107.
Selvadurai, A. P. S., & Kim, J. (2016). Poromechanical behaviour of a surficial geological barrier during fluid injection into an underlying poroelastic storage formation. *Proceedings of the Royal Society A, 472*, Article 20150418.
Selvadurai, A. P. S., & Mahyari, A. T. (1997). Computational modeling of the indentation of a cracked poroelastic half-space. *International Journal of Fracture, 86*, 59–74.
Selvadurai, A. P. S., & Najari, M. (2017). The thermo-hydro-mechanical behavior of the argillaceous Cobourg Limestone. *Journal of Geophysical Research: Solid Earth, 122*, 4157–4171.
Selvadurai, A. P. S., & Nguyen, T. S. (1995). Computational modelling of isothermal consolidation of fractured porous media. *Computers and Geotechnics, 17*, 39–73.
Selvadurai, A. P. S., & Nguyen, T. S. (1997). Scoping analyses of the coupled thermal-hydrological-mechanical behaviour of the rock mass around a nuclear fuel waste repository. *Engineering Geology, 47*, 379–400.
Selvadurai, A. P. S., & Samea, P. (2020). On the indentation of a poroelastic halfspace. *International Journal of Engineering Science, 149*, Article 103246.
Selvadurai, A. P. S., & Shirazi, A. (2004). Mandel-Cryer effects in fluid inclusions in damage-susceptible poroelastic geologic media. *Computers and Geotechnics, 31*, 285–300.
Selvadurai, A. P. S., Singh, B. M., & Au, M. C. (1996). The matrix-fiber crack in an elastic solid. *Journal of Applied Mechanics, 118*, 639–649.
Selvadurai, A. P. S., & Suvorov, A. P. (2012). Boundary heating of poro-elastic and poro-elasto-plastic spheres. *Proceedings of the Royal Society A, 468*, 2779–2806.
Selvadurai, A. P. S., & Suvorov, A. P. (2014). Thermo-poromechanics of a fluid-filled cavity in a fluid-saturated geomaterial. *Proceedings of the Royal Society A, 470*, Article 20130634.
Selvadurai, A. P. S., & Suvorov, A. P. (2016). *Thermo-poroelasticity and geomechanics*. Cambridge University Press.
Selvadurai, A. P. S., & Suvorov, A. P. (2016). Coupled hydro-mechanical effects in a poro-hyperelastic material. *Journal of Mechanics and Physics of Solids, 91*, 311–333.
Selvadurai, A. P. S., Willner, K., & Gaul, L. (2005). On frictionally constrained wing cracks. *Archives of Mechanics, 57*, 133–151.
Selvadurai, A. P. S., Zhang, D., & Kang, Y. (2018). Permeability evolution in natural fractures and their potential influence on loss of productivity in ultra-deep gas reservoirs of the Tarim Basin, China. *Journal of Natural Gas Science and Engineering, 58*, 162–177.
Selvadurai, A. P. S., Selvadurai, P. A., & Suvorov, A. P. (2018). Contact mechanics of a dilatant region located at a compressed elastic interface. *International Journal of Engineering Science, 133*, 144–168.
Shah, S. P., & Swartz, S. E. (Eds.). (1989). *Fracture of concrete and rock*. Berlin: Springer-Verlag.
Shah, S. P., Swartz, S. P., & Barr, B. (Eds.). (1989). *Fracture of concrete and rock. Recent developments*. London: Elsevier Applied Science.
Shen, B., Stephansson, O., & Rinne, M. (2014). *Modelling rock fracture processes. A fracture mechanics approach using FRACOD*. Berlin: Springer-Verlag.
Shih, C. F., De Lorenzi, H. G., & German, M. D. (1976). Crack extension modeling with singular quadratic isoparametric elements. *International Journal of Fracture, 12*, 647–651.
Sih, G. C., & Chen, E. P. (1981). Cracks in composite materials, mechanics of fracture *6*. The Hague: Martinus Nijhoff Publishers.
Sih, G. C. (1991). *Mechanics of fracture initiation and propagation*. Dordrecht, The Netherlands: Kluwer Academic Publishers.
Sinclair, G. B. (2004a). Stress singularities in classical elasticity-I: Removal, interpretation and analysis. *Applied Mechanics Reviews, 57*, 251–298.
Sinclair, G. B. (2004b). Stress singularities in classical elasticity-II: Asymptotic identification. *Applied Mechanics Reviews, 57*, 385–439.
Smith, B. M. (2015). *Hydraulic fracturing*. Boca Raton, FL: CRC Press.
Sneddon, I. N. (1946). The distribution of stress in the neighbourhood of a crack in an elastic solid. *Proceedings of the Royal Society of London. Series A, 187*, 229–260.
Sneddon, I. N. (1951). *Fourier transforms*. New York, McGraw-Hill.
Sneddon, I. N. (1965). A note on the problem of the penny-shaped crack. *Mathematical Proceedings of the Cambridge Philosophical Society, 61*, 609–611.
Sneddon, I. N., & Lowengrub, M. (1969). *Crack problems in the classical theory of elasticity*. John Wiley & Sons.
Song, Y., Hu, H., & Rudnicki, J. W. (2017). Dynamic stress intensity factor (Mode I) of a permeable penny-shaped crack in a fluid-saturated poroelastic solid. *International Journal of Solids and Structures, 110*, 127–136.
Speight, J. G. (2016). *Handbook of hydraulic fracturing*. New York: John Wiley & Sons, Inc..

Spencer, A. J. M. (1965). On the energy of a Griffith crack. *International Journal of Engineering Science, 3*, 441–447.
Srivastava, K. N., & Singh, K. (1969). The effect of penny-shaped crack on the distribution of stress in a semi-infinite solid. *International Journal of Engineering Science, 7*, 469–490.
Sternberg, E. (1958). Three-dimensional stress concentrations in the theory of elasticity. *Applied Mechanics Reviews, 11*, 1–4.
Suvorov, A. P., & Selvadurai, A. P. S. (2019). The Biot coefficient for an elasto-plastic material. *International Journal of Engineering Science, 145*, Article 103166.
Terzaghi, K. (1925). *Erdbaumechanik auf bodenphysikalischer grundlage*. Vienna: Franz Deuticke.
Tsang, Y. W., Birkholzer, J. T., & Mukhopadhyay, S. (2009). Modeling of thermally driven hydrological processes in partially saturated fractured rock. *Reviews of Geophysics, 47*, 1–30.
Valko, P., & Economides, M. J. (1996). *Hydraulic fracture mechanics*. New York: John Wiley.
Verruijt, A. (2015). *Theory and problems of poroelasticity*. The Netherlands: Delft University of Technology.
Wang, H. F. (2000). Theory of linear poroelasticity with applications to geomechanics and hydrogeology *(Vol. 2)*. Princeton University Press.
Westergaard, H. M. (1939). Bearing pressures and cracks. *Journal of Applied Mechanics, 6*, 49–53.
Williams, B. B. (1970). Fluid loss from hydraulically induced fractures. *Journal of Petroleum Technology, 249*, 882–888.
Willis, J. R. (1967). A comparison of the fracture criteria of Griffith and Barenblatt. *Journal of the Mechanics and Physics of Solids, 15*, 151–162.
Yi, L. P., Waisman, H., Yang, Z. Z., & Li, X. G. (2020). A consistent phase field model for hydraulic fracture propagation in poroelastic media. *Computer Methods in Applied Mechanics and Engineering, 372*, Article 113396.
Yue, Z. Q., & Selvadurai, A. P. S. (1995). On the mechanics of a rigid disc inclusion embedded in a fluid-saturated poroelastic medium. *International Journal of Engineering Science, 33*, 1633–1662.
Yue, Z. Q., Selvadurai, A. P. S., & Law, K. T. (1994). Excess pore pressure in a poroelastic seabed saturated with a compressible fluid. *Canadian Geotechnical Journal, 31*, 989–1003.
Zhang, J. (2013). Borehole stability analysis accounting for anisotropies in drilling to weak bedding planes. *International Journal of Rock Mechanics and Mining Sciences, 60*, 160–170.
Zheltov, Y. P., & Khristianovitch, S. A. (1955). Hydraulic fracture of an oil-bearing bed. *Izvestiya Akademii Nauk, 5*, 3–41.
Zienkiewicz, O. C., & Shiomi, T. (1984). Dynamic behaviour of saturated porous media; the generalized Biot formulation and its numerical solution. *International Journal for Numerical and Analytical Methods in Geomechanics, 8*, 71–96.